2013•2014
FACULTEIT GENEESKUNDE EN LEVENSWETENSCHAPPEN
master in de biomedische wetenschappen

Masterproef

Synthesis and in situ characterization of graphene on copper substrates

Promotor :
Prof. dr. Hans-Gerhard BOYEN

Copromotor :
Prof. dr. Milos NESLADEK

Lien Callens

Proefschrift ingediend tot het behalen van de graad van master in de biomedische wetenschappen

De transnationale Universiteit Limburg is een uniek samenwerkingsverband van twee universiteiten in twee landen: de Universiteit Hasselt en Maastricht University.

universiteit hasselt
KNOWLEDGE IN ACTION

Universiteit Hasselt | Campus Hasselt | Martelarenlaan 42 | BE-3500 Hasselt
Universiteit Hasselt | Campus Diepenbeek | Agoralaan Gebouw D | BE-3590 Diepenbeek

universiteit hasselt | Maastricht University

2013•2014
FACULTEIT GENEESKUNDE EN LEVENSWETENSCHAPPEN
master in de biomedische wetenschappen

Masterproef

Synthesis and in situ characterization of graphene on copper substrates

Promotor :
Prof. dr. Hans-Gerhard BOYEN

Copromotor :
Prof. dr. Milos NESLADEK

Lien Callens

Proefschrift ingediend tot het behalen van de graad van master in de biomedische wetenschappen

universiteit hasselt | Maastricht University

Acknowledgment

First of all I would like to thank the people that helped me with my thesis project and this senior internship. It was a real pleasure, and great fun.

Being part of the Nano Structure Physics (NSP) group of Prof. Hans-Gerd Boyen has been one of the most knowledge building as well as challenging experiences in my academic journey. I thank him for providing guidance and advice in this low-dimension physics world. I also want to thank my copromotor Prof. dr. Milos Nesladek (Wide bandgap materials group) and the Institute for Materials Research (IMO) for giving me the opportunity to execute this interesting project.

I came to the Institute of Materials Research as a master student. Although I acquired some research experience before, I was completely new to the field of carbon nanomaterials. The NSP group members really helped me during this discovery. Prof. Boyen was a true interpreter, translating quantum physics in a way he handed Christopher and me the red pill that opened our eyes for the potential of wonderland. Showing us how deep the rabbit hole goes, while all he was explaining is the “invisible” truth and nothing more. By working together with Christopher Freiwald, drs. Joris Artois and dra. Tanya Jacobs in one group I have developed a liking towards collaborative research. Everybody’s ideas and opinions were heard and valued equally, when adaptations needed to be made on the set-up of our used systems. I would also like to thank Joris and Tanya for their time, for helping me with the atomic force microscopy measurements and for fine-tuning this thesis manuscript.

I wish to acknowledge the help provided by drs. Giedrius Degutis (Inorganic and Physical Chemistry), for performing Raman measurements on my samples. Also I am particularly grateful for the assistance given by Johnny Baccus. By helping me with some of the used set-ups, I became a lot handier during this internship.

I found good friends in Sören Kuypers, Mandy Berden and my partner in crime Christopher. They will agree that this senior internship could be a drama sometimes; luckily there were also many joyful moments. They supported me and shared my successes and excitement. I always brightened up from some card games during lunch or a delicious hot coco at coffee café.

Finally, I would also like to thank my friends, family and boyfriend for their support and patience. They listened, helped and cheered me up when that was needed.

Lien Callens
Instituut voor Materiaal Onderzoek
June 10, 2014

Content

Abbreviations

0D	Zero dimension
1D	One-dimensional
2D	Two-dimensional
3D	Three-dimensional
AFM	Atomic force microscopy
CH_4	Methane
CHA	Concentric hemispherical analyser
Cu	Copper
CVD	Chemical vapor deposition
EELS	Electron energy loss spectroscopy
ESCA	Electron spectroscopy for chemical analysis
FET	Field effect transistor
FWHM	Full width at half-maximum
GFET	Graphene field effect transistor
H_2	Hydrogen
He	Helium
HOPG	Highly ordered pyrolytic graphite
PE	Pass energy
PS	Photoelectron spectroscopy
QHE	Quantum Hall effect
RS	Raman spectroscopy
SET	Single electron transistor
UHV	Ultrahigh vacuum
UPS	Ultraviolet photoelectron spectroscopy
XPS	X-ray photoelectron spectroscopy
ZLP	Zero loss peak

Abstract – English

This thesis project focuses on the study of graphene, a rising star in materials science with many applications in (bio)electronics, photonics, bioengineering and biosensors. Graphene monolayers and bilayers possess unique characteristics due to their two-dimensional crystal structure. However, a controlled synthesis of graphene monolayers or bilayers on a wafer-size scale remains a challenge.

This project makes the first step towards the in situ preparation and characterization of graphene, on suitable copper substrates. Bilayer and even single layer graphene films were formed using chemical vapor deposition with methane and hydrogen precursors and Cu foils as catalyst. Previous studies have shown that chemical vapor deposition is the most efficient method for synthesis of large area graphene crystals. The graphene growth process executed under ultrahigh vacuum conditions was chemically analysed exploiting different spectroscopic techniques.

X-ray photoelectron spectroscopy, ultraviolet photoelectron spectroscopy and electron energy loss spectroscopy were used to characterise the films during the different growth steps. These results were compared with the results of ex situ Raman spectroscopy and atomic force microscopy measurements to check the quality and the morphology of the graphene samples formed on Cu films. With these experiments we tried to understand the fundamental growth mechanism and catalyst interaction to establish a method for a controlled growth. We also examined the influence of ambient conditions on the properties of graphene. This influence was studied by comparing in situ results with electron spectroscopic data acquired after exposing the samples to ambient conditions for different times. Gaining insight in how graphene samples react to post growth ambient air exposure plays an important factor for the correct use of graphene in experiments or applications. Finally, surface treatments were applied to reverse the impact of air-based contaminations while simultaneously trying to avoid extensive damage to the sample morphology. During these thermal treatments graphene was annealed under ultrahigh vacuum conditions at elevated temperatures. We found that heating to 773 K for five minutes only removed part of the contaminations, while annealing to 973 K allowed to basically restore the original state of a sample.

This controlled synthesis together with the acquired knowledge of how graphene interacts with its environment and how we can reverse this environmental influence will create opportunities for the use of graphene application wise.

Keywords: Chemical vapor deposition, graphene on copper samples, Raman spectroscopy, atomic force microscopy, x-ray photoelectron spectroscopy, electron energy loss spectroscopy, ultraviolet photoelectron spectroscopy, ambient air exposure, thermal treatment.

Abstract – Nederlands

Deze master thesis draait rond de studie van grafeen, een opkomend fenomeen in de materiaalkunde. Grafeen monolagen en dubbellagen bezitten door hun unieke tweedimensionale kristalstructuur enkele speciale eigenschappen. Deze eigenschappen zorgen ervoor dat grafeen potentieel heeft voor nieuwe applicaties in de (bio)elektronica, fotonica, biotechnologie en biosensoren. Helaas is er nog steeds veel onwetendheid betreffende de eigenschappen en het potentieel waarover grafeen beschikt. Daarnaast blijft het tot vandaag een uitdaging om grafeen op grote schaal gecontroleerd te produceren.

Dit master thesis project zet een eerste stap naar de synthese en de karakterisering van grafeen gevormd op koperen substraten. Door gebruik te maken van een “chemical vapor deposition” proces hebben we enkel gelaagd en dubbel gelaagde grafeen films geproduceerd uitgaande van waterstof, methaan gassen en een koper film als katalysator. Het productieproces van grafeen werd uitgevoerd onder ultrahoog vacuüm en nadien werden de films geanalyseerd met verschillende spectroscopische technieken. X-ray foto-elektron spectroscopie, UV-foto-elektron spectroscopie en elektronen energieverlies spectroscopie werden gebruikt om de film op verschillende groeistappen te karakteriseren. Deze resultaten werden vergeleken met de resultaten van ex situ Raman spectroscopie en atomic force microscopie, om de kwaliteit en de morfologie van de gevormde grafeen stalen te controleren. We hebben geprobeerd om inzicht te verwerven in het fundamenteel groei mechanisme van grafeen en de interacties tussen grafeen en het koper substraat. We hebben ook onderzocht of er veranderingen optreden in onze grafeen film nadat ze zijn blootgesteld aan een atmosferische druk. Dit effect werd geanalyseerd door onze in situ metingen van een grafeen staal te vergelijken met ex situ metingen van het identieke staal na blootstelling. Tot slot, hebben we twee behandelingen uitgetest om de geabsorbeerde luchtvervuilingen te verwijderen van het grafeen oppervlak. Tijdens de eerste behandeling werden de stalen 5 min verwarmd op 773 K en de temperatuur bereikte 993 K tijdens de tweede behandeling. We ondervonden dat de eerste behandeling maar een deel van de contaminaties verwijderde. De tweede behandeling, waar de temperatuur 973 K bereikte, slaagden we er wel in al deze contaminaties te verwijderen. Een nadeel aan deze methode was echter dat Raman spectroscopie aantoonde deze behandeling kleine defecten veroorzaakte in onze grafeen lagen.

Kortom, tijdens dit project zijn we erin geslaagd grafeen monolagen en dubbellagen op koper substraten te produceren. We analyseerden het effect van blootstelling aan lucht en toonden aan dat grafeen luchtcontaminaties absorbeert op het oppervlak. Deze verontreinigingen werden op hun beurt verwijderd door de stalen thermisch te behandelen. Deze gecontroleerde synthese samen met de verworven kennis van hoe grafeen verandert in een atmosferische omgeving levert ons nieuwe kennis over hoe we grafeen correct moeten gebruiken of voorbehandelen voor applicaties.

Sleutelwoorden: Chemical vapor deposition, grafeen op koper substraten, Raman spectroscopie, atomic force microscopie, x-ray foto-elektron spectroscopie, UV-foto-elektron spectroscopie en elektronen energieverlies spectroscopie, blootstelling aan atmosferische druk, thermische behandeling.

Chapter 1

Introduction

In 2004 Andre Geim and Kostya Novoselov were the first to extract graphene from bulk graphite and since then graphene has attracted a great deal of attention. This one carbon atom thick sheet has a two-dimensional (2D) hexagonal crystal structure and possesses outstanding mechanical, thermal and chemical properties. Due to these unique properties, graphene offers new ways into low-dimensional physics and continues to provide a fertile ground for applications. High carrier mobility, high thermal conductivity, tuneable band gap, visible transparency and a robust structure are some of the main characteristics of graphene [1-5]. Table 1 summarizes several potential applications for graphene that are under development. Electronics, photonics and optoelectronics are particular areas where graphene will be used in the future on a commercial scale and they are explained in more detail below [6].

This project gives a view on new aspects regarding graphene synthesis: the fundamental growth mechanism, catalyst graphene interaction and influence of post growth ambient exposure. By searching for the right synthesis variables, a controllable growth of single and bilayer graphene films is obtained. This controlled synthesis together with the acquired knowledge of how graphene interacts with its environment and how we can reverse this environmental influence will create opportunities for the use of graphene, application wise.

Table 1: Main application for graphene with its physical properties adapted from (http://2-dtech.com/applications/).

Application	Properties graphene
Bendable electronics Touch screens E-paper Foldable OLED	Transmittance (97.7%)
Transistors	High mobility High on/off ratios (10^6 for vertical devices) High cut off frequencies (up to 1 THz)
Photonics Photodetectors Optical modulators Opitical polarization controllers	 Wavelength independent absorption Large bandwidth operation Good extinction ratios in magnetic fields
Sensors	High sensitivity Multifunctional sensing (strain, gas environment, magnetic field etc.) Universal resistance standard based on easily observable quantum Hall effect
Bioapplications	Large surface area Chemical purity Easy functionalization

The aim of this thesis project is to produce high-quality graphene layers on top of Cu substrates and to investigate the influence of oxygen after ambient air exposure. The project comprises two parts. In the first part, graphene samples were synthesized by means of chemical vapor deposition (CVD). The basics of the applied CVD processes are explained in more detail below. Different analysis techniques like x-ray photoelectron spectroscopy (XPS), ultra violet photoelectron spectroscopy (UPS), Raman spectroscopy (RS) and electron energy loss spectroscopy (EELS) are used for characterization. Also, the film quality, the chemical, electronic and vibrational properties of the resulting graphene layers are analysed. In addition, their morphology is studied using atomic force spectroscopy (AFM) [7, 8]. The chemical analysis will lead to the determination of appropriate growth parameters and, thus, towards a controlled synthesis process. In the second part, the influence of ambient conditions ('ex situ') on graphene layers is examined. The chemical composition of the as-grown graphene samples will be measured in situ with XPS, UPS and EELS. Next, identical measurements were performed on the samples after air exposure. The results from in situ and ex situ measurements are used to define changes in the chemical character of the graphene samples. The few layer graphene is expected to react with different molecules in the air. These molecules might influence the properties of the graphene by chemical interaction thereby forming chemical and/or physical bonds. By comparing the results of in situ an ex situ measurements the shift in the chemical character upon exposure to air is investigated. This chemical shift can also contribute to a better understanding of the growth mechanism and interactions between the Cu substrate and the graphene [9].
The possibility to reverse the impact of contaminations is explored as a last experiment in this thesis. The graphene sample undergoes thermal annealing for five minutes at 773 K and 973 K to remove the unwanted molecules from its surface without causing damage to the morphology of the 2D crystal structure [10].

1.1 Structure of graphene

Until 2004 there was no experimental prove that strictly two-dimensional (2D) materials could exist without a three-dimensional (3D) support. 2D materials were thought to be thermodynamically unstable, their melting point decreases with a decrease of layer thickness. This theory of Landau and Peierls, which was overall accepted for more than 70 years, was proven wrong by a "Friday night experiment" in the University of Manchester. In this experiment a 2D crystal structure named graphene was derived by the now famous "scotch tape method" [2].
Graphene can be described as a flat monolayer of carbon atoms tightly packed into a 2D honeycomb lattice. It is also the basic building block for all other graphitic materials shown in Figure 1. Stacked graphene forms the well-known graphite (3D), while rolled or wrapped graphene forms (1D) carbon nanotubes or (0D) fullerenes [2-6].

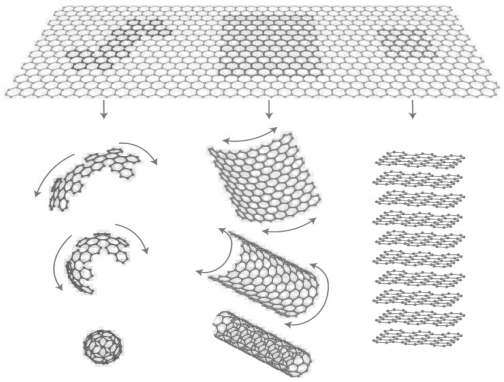

Figure 1: Graphene structure is a simple planar hexagonal arrangement of carbon atoms and it can be used as a basic structure to form (0D) fullerenes, (1D) carbon nanotubes and (3D) graphite (2).

Graphene is a 2D sheet of hexagonally arranged carbon and has sp^2 hybridized orbitals with the adjacent carbon atoms. These orbitals form the three σ-bonds within a planar 120° configuration having about 1.4 angstroms as interatomic distance. This makes the bond between the neighbouring atoms within one graphene layer quite strong. Within the honeycomb lattice, there are two possible cuts, the “armchair” and “zig-zag”. These two main directions in the crystal lattice show a different electronic behaviour [4, 5].

In graphite, the graphene layers are only weakly coupled with the p_z orbital, they form bonding π and anti-bonding π* states and the sheet are separated by a distance of about 3.4 angstroms [11, 12].

1.2 Electrical properties

The fact that graphene exhibits new physical phenomena, has played a major role in the graphene gold rush over the last years. In the next paragraph some major aspects of graphene physics are addressed. They demonstrate the great interest in fundamental research on graphene for future electronic applications. Some of the most interesting applications will also be mentioned at the end of this part.

An important fact in graphene production is that the electronic structure of graphene is very dependent on the amount of layers. Only single and double layer graphene have simple electronic properties that classify these 2D crystals as zero-gap semiconductors. This differentiates them from multilayer graphene or graphite because these do not possess a linear dispersion relation, which is the fundamental basis of the electronic properties of single and double layer graphene [5].

Figures 2.A represents the low-energy band structure of graphene, illustrated by two symmetric cones. The valence band is formed by π-bonding states previously mentioned. While the conduction band is formed by the anti-bonding π* states. These states are orthogonally positioned, touching at six points. These connecting points are called Dirac points. Due to the fact that graphene is an exception to the Schrödinger equation, the electronic properties of graphene are better described using the Dirac equation. This Dirac Hamiltonian is used to define the electrons present in graphene representing low energy quasiparticles. These quasiparticles are also called massless Dirac fermions and they can be seen as electrons with effective mass zero [2, 4, 13].

The unit cell of graphene, shown in Figure 2.B, contains two carbon atoms and the graphene lattice is divided in two sub-lattices, A and B evolving from the two carbon atoms [2, 13, 14].

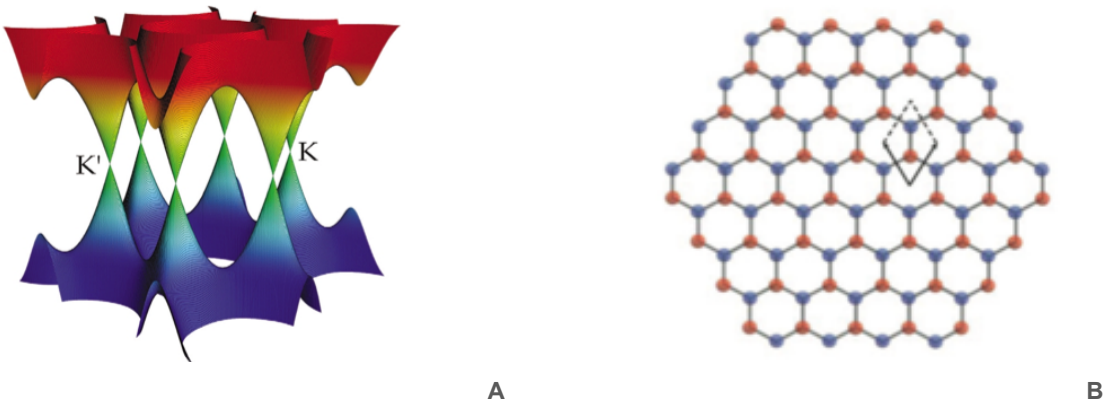

Figure 2: (A) The band structure of single and double layer graphene. The figure shows that the conduction bands touch the valence bands at the Dirac points (4). (B) The crystal structure of graphene with its different sublattices A and B marked in blue and red (5).

The previously discussed band structure is responsible for different transport phenomena in graphene. Three of the most important features are the minimum conductivity, high carrier mobility and quantum Hall effect.
As stated before, single and bilayer graphene possess a band gap width wide zero and therefore the type of charge carrier is determined by the position of the Fermi energy. This Fermi energy level can be tuned by applying a voltage or an electrical field as provided by a gate voltage V_g. Figure 3.A illustrates this pronounced ambipolar electrical field effect in graphene and a direct consequence is the strong dependence of the conductivity on the gate voltage. By sweeping the gate voltage Vg from -60 V to +60 V the Fermi energy level shifts from the valence band (on the left) to the conduction band (on the right). This phenomenon affects charge carrier density, resistivity and simultaneously, the conductivity. A minimal however finite value of conductivity is reached at the Dirac point, also referred to as charge neutrality point. Studies have shown that the conductivity in graphene never falls below a certain value. The charge carriers in graphene can be tuned continuously between electrons and holes in concentrations n as high as 10^{-13} cm^{-2}. Their mobilities μ can exceed 15.000 cm^2 V^- s^- under ambient conditions and they can reach 100.000 cm^2 V^- s^- at 300 K. This extraordinary high carrier mobility is almost not affected by chemical doping. Therefore graphene can be used for ballistic transport on the submicroscopic scale [2, 4, 5].

Besides a high mobility and minimum conductivity graphene also has an interesting anomalous quantum Hall effect (QHE). This QHE is directly related to the previously mentioned massless Dirac electrons. Future description of the QHE goes beyond the scope of this thesis but can be found in many reviews or experimental studies [2].

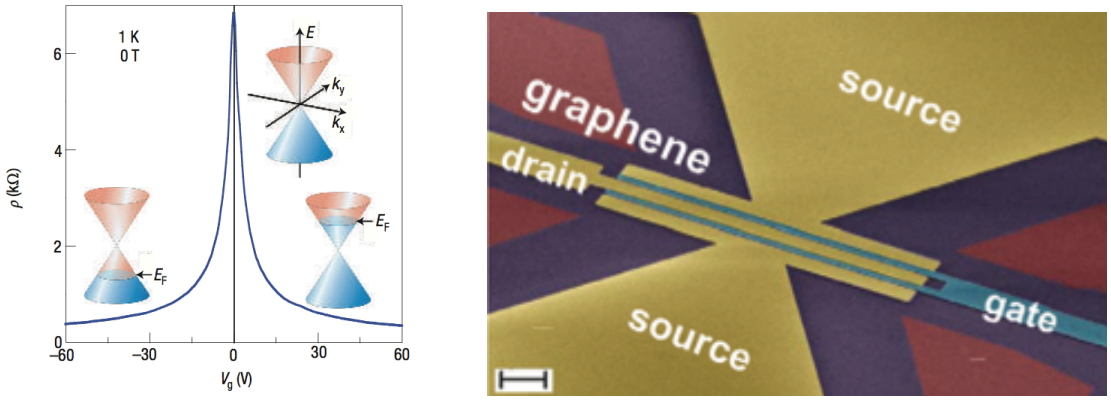

A B

Figure 3: (A) Ambipolar electric field effect of graphene shows how the position of the Fermi energy Ef is dependent on the applied gate voltage Vg. A positive Vg will result in electrons, while a negative voltage will form holes. The resistivity will also rapidly decrease, more or less independently of the temperature when charge carriers are added. This is an indication of the high mobility (2). (B) Optical microscope of a graphene based FETs (5).

These outstanding electronic properties make graphene a promising material for many future applications in electronics. Graphene is a very good candidate as channel material for field effect transistors (FETs). These graphene field effect transistors (GFETs), shown in Figure 3.B, do need the introduction of an energy gap to become a semiconductor. GFETs perform well at low temperatures, up to 4 K. This makes them ideal for operation under extreme environments like space. To build graphene transistors an insulating material is needed and 2D boron nitride (BN) crystals are proven to be ideal for this job. BN films have a large bandgap of 6 eV making them ideal for gate insulator and substrate in GFETs. Graphene can also be used as a conduction sheet to create single electron transistors (SET). Components as conducting channels, interconnects and barrier can all be cut from single graphene layers. The high conductivity of graphene and large surface to volume ratio make it also an excellent candidate for electric batteries [2, 5].

1.3 Optoelectronic and other properties

Apart from unique electrical properties graphene also possesses outstanding optical properties, such as the fact that a single graphene layer is still visible without an AFM despite it being the thinnest material even made. Recently, wide energy range studies demonstrated that graphene monolayers absorbs 2.3 % or even more of the light that passes through it. Another characteristic of graphene layers is that they produce a photocurrent upon photoexcitation. This, together with a wide absorption range, the ability to work at ambient temperature, their thinness and high carrier mobility makes them ideal photodetectors.

Besides, single and bilayer graphene also have a fast decay time after excitation. Due to this the light absorption of graphene decreases with an increase in intensity without causing damage and therefore it can be used in laser cavities to produce picosecond laser pulses from a continuous wave output [2, 5].

1.4 Chemical vapor deposition

The properties of graphene depend strongly on the thickness or the number of layers. In the case of multiple layers the characteristics will change, which is an issue in graphene based technologies. Therefore the synthesis of large-scale few layer graphene films of high quality is of great importance [6, 15]. Various approaches have been developed to produce single or double/triple layered graphene, such as mechanical exfoliation, chemical reduction of graphene oxides and chemical vapor deposition (CVD) [16, 17]. CVD combined with a copper (Cu) catalyst has been recognised as a promising method to synthesize large area graphene monolayers. Sukang Bae et al. even reported production of 30 inch monolayer graphene on flexible Cu foils by a roll-to-roll production method [18].

During CVD a substrate is exposed to certain volatile precursors and chemical reactions of these vapor species will cause the deposition of a thin solid film on the substrate. Figure 4 shows the simple CVD set-up with the different components: the reactor with the heaters, the gas delivery system with the mass flow controllers, the valves and finally a gas removal system. During a thermal CVD experiment the temperature will be increased in the reactor until the required growth temperature is reached. When this temperature is reached the flow rate of the reactive gas species is set and the chemical reaction will take place in the reactor. The graphene films will form in the reactor and the non-reacted gases and the byproducts are removed by vacuum pumps.

For the graphene synthesis, Cu is used as substrate and methane (CH_4) is exploited with or without additional hydrogen (H_2) as precursors. Thermal CVD can be executed at different pressures, atmospheric pressure, low-pressure or ultrahigh vacuum (UHV). The CVD processes used for this thesis are executed in high vacuum [15, 19].

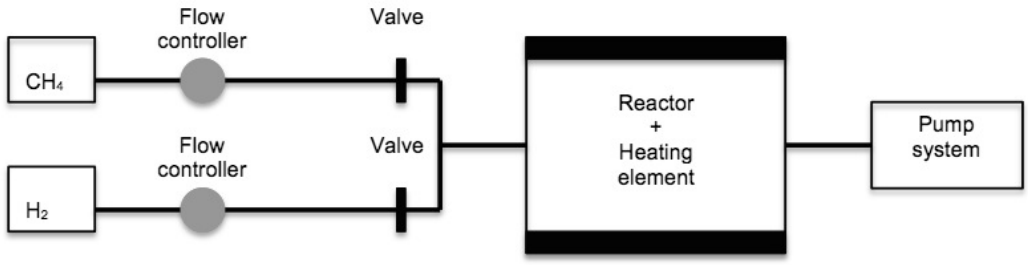

Figure 4: Schematic representation of the CVD set-up with the different components: the vapor species flows are regulated by the mass flow controllers, the temperature in the reactor is regulated by the heating element and the vacuum system powered by the different pumps removes the exhaust gases.

CVD depends on various parameters such as the pressure, the temperature, the chemical reaction time and the flow rate [20]. Figure 5 illustrates the influence of the transport kinetics of the vapor species in a CVD experiment. In this experiment the Cu substrate is used as catalyst, the catalyst will contribute to the graphene deposition by lowering the energy barrier of the reaction. A lower energy barrier will cause dissociation of the vapor precursors and formation of the graphitic structures. The use of a catalyst will enhance the reaction kinetics resulting in a better control of the graphene quality [19, 21].

Many metal catalysts can be used for graphene production and the use of Cu catalyst has certain advantages. Cu has a very low carbon solubility (< 0,1 atom %) even at high synthesis temperatures. So, graphene growth on Cu

is a surface mediated process and the formation of precipitations by dissolution is negligible. This leads to a better control over the amount of formed graphene layers and in that way producing the high quality few layer graphene. Another advantage of Cu catalyst is that it has a lower catalytic capability then Ni catalyst. This also leads to a more controlled CVD process of graphene synthesis [19].

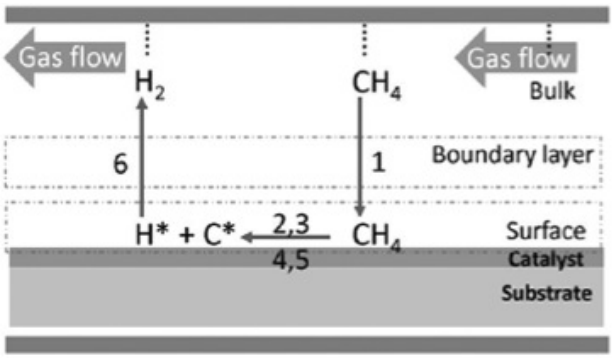

Figure 5: The different processes involved during the chemical deposition process of graphene. In this diagram the reactants first diffuse trough the boundary layer (1), then they are absorbed on the substrate surface (2). Next, chemical reactions will decompose the vapor species in active carbon and reactive hydrogen species (3). These active carbon species will form the graphene layer (4); the byproducts (hydrogen) and non-reacted gases will diffuse away from the substrate surface (5). After they diffused trough the boundary layer they will be removed from the reactor by the vacuum pumps (21).

Figure 5 summarises how graphene grows on Cu. First, the Cu substrate is exposed to the chosen precursors; hydrogen and methane gases. In the next step these vapor species will be decomposed on the Cu surface to form active carbon species. These active carbon species can form graphene nuclei. The formation of graphene islands and finally the coverage of the Cu sample with graphene will depend on the used temperature, precursor partial pressures and the Cu surface quality. The inactive species, hydrogen and non-reacted carbon will diffuse from the surface through the boundary layer and are eventually removed by the vacuum pumps [21].

Chapter 2

Experimental

In this chapter, the experimental techniques relevant to this thesis are introduced. This project involves the synthesis of graphene by CVD. A detailed description of the CVD process and the involved materials will be given in the next section. Chemical analysis of the resulting graphene samples was performed using Raman Spectroscopy, XPS, EELS and UPS measurements. AFM measurements were made on the samples in order to study the surface morphology of the graphene on the Cu sample.

2.1 Chemical vapor deposition process

The graphene samples made in this thesis were grown on 25 μm thick Cu foils, 99.999% (Alfa Aesar, NO. 10950, metal basis). This foil was cut into samples of ~1cm^2 to fit into the heating cylinder in the reactor. The Cu substrates were heated in the reactor at a typical temperature of 1200 K and a base pressure of 10^{-8} mbar. During the annealing step, hydrogen (ALPHAGAZ, H_2, 99.9999%) was added with a typical flow rate of 35 sccm. Methane (ALPHAGAZ, CH_4, N55 99.9995%) was added during the growth step. After growth, the chamber was cooled from the growth temperature to 673 K with 50 sccm of hydrogen. Below 673 K, the cooling continued without gas flow in ultrahigh vacuum conditions. The used CVD process and the different steps for the formation of graphene in this thesis is illustrated in Figure 6.

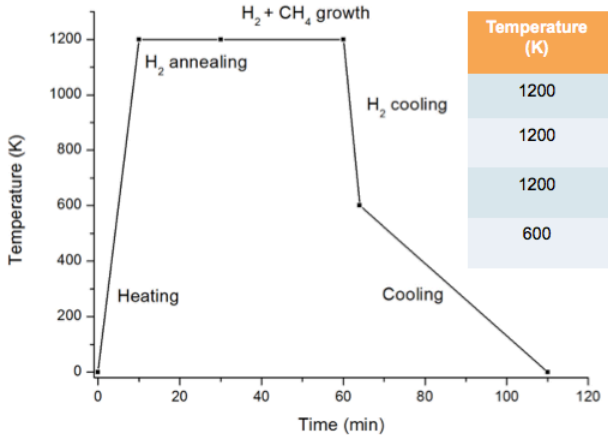

Temperature (K)	Time (min)	Gas Flow (sccm)	Process
1200	10	X	Heating
1200	20	35 H_2	Annealing in H_2
1200	30	50 H_2 / 20 CH_4	Growing
600	4	35 H_2	Cooling in H_2

Figure 6: Schematic representation of the used CVD process, it illustrates the temperature-time profile for the different CVD steps.

After the CVD step the produced graphene samples were characterized in situ using XPS, UPS, EELS and ex situ by means of Raman spectroscopy. These measurements were performed to prove the presence of graphene layers on the Cu substrate and to detect possible contaminations. An overview of the different CVD processes used for each sample is included in the appendix in Table 5. Two surface treatments were also tested to remove the contaminations due to air exposure. We heated the graphene samples under UHV for five minutes. The temperature reached 773 K during the first treatment and 973 K during the second one.

2.2 Surface analysis: Photoelectron spectroscopy

Photoelectron spectroscopy (PS) measures the energy of the electrons ejected from liquids, gases and solids by the photoelectric effect, which is explained in section 2.3. This energy measurement of the electrons determines the binding energy (BE) of the electrons in the sample. Ultraviolet photoelectron spectroscopy and x-ray photoelectron spectroscopy are two techniques based on photoelectric effect that are commonly used for qualitative and quantitative surface analysis. Since UPS uses ultraviolet light to excite electrons there is only sufficient energy to emit electrons from the valence band. Therefore UPS is widely used in the study of the electronic band structure of metals, alloy, semiconductors and adsorption phenomena. For core level electrons on the other hand much higher photon energies are required to remove them from the atoms. As these energies typically lie in the x-ray regime of the electromagnetic spectrum, the photoelectron spectroscopy of core levels is commonly known as XPS or electron spectroscopy for chemical analysis (ESCA) [22, 23].

Table 2: Possible applications for XPS and UPS adapted from (http://chemwiki.ucdavis.edu/Physical_Chemistry /Spectroscopy/Photoelectron_Spectroscopy/Photoelectron_Spectroscopy%3A_Application).

Application	XPS	UPS	Application	XPS	UPS
Materials on surfaces	X	X	Electron energy levels	X	X
Depth profiling	X		Elemental composition	X	
Angle dependent studies	X	X	Valence band fine structure		X
Binding energy	X	X	Oxidation states or adsorption sites	X	

The main goal in UPS or XPS is to gain information about the chemical state, composition, electronic state, and binding energy of the analysed surface. The key point in PS is that a lot of qualitative and quantitative information about the surface region of solids can be obtained. Specifics about what can be studied using XPS or UPS is summarized in Table 2.

2.2.1 Photoelectron instrumentation

A photoelectron spectrometer needs a few basic components in the instrumental set-up, which are represented in Figure 7.A. These include an UHV environment, a radiation source and an energy analyser. The ejected electrons travelling from the sample surface towards the energy analyser should encounter as few gas molecules as possible, otherwise they will be scattered and lost from the analysis. For most experiments it is adequate to operate at a base pressure of the order of 10^{-9} mbar or below.

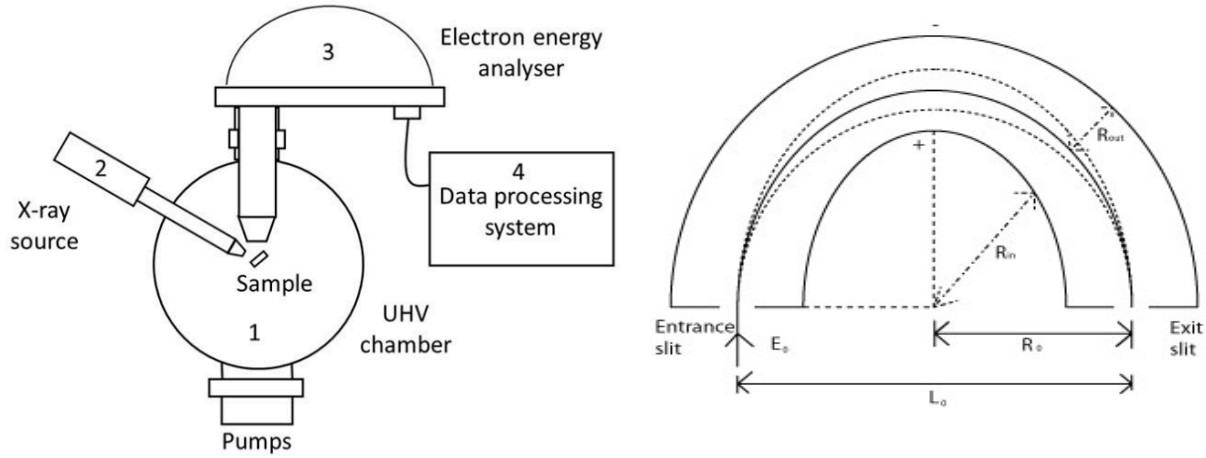

Figure 7: (A) Typical set-up of PS instrumentation used in XPS and UPS with the basic elements. (B) Schematic representation of a concentric hemispherical analyser (CHA). Only photoelectrons of the correct energy are able to pass through the detector instead of colliding with the side walls of the hemisphere (23).

The radiation sources used in UPS and XPS are fixed-energy radiation sources. The used sources as well as the used analysers are discussed in more detail below [22, 23].

2.2.2 Radiation sources

While many components of instruments used in PS are common to both UPS and XPS, the radiation sources are one area of distinction. The radiation source for UPS is a gas discharge lamp, with the typical one being a Helium (He) discharge lamp allowing excitation energies of 21.2 or 40.8 eV, respectively.

The used x-ray source is determined by two important factors. The energy of the x-ray has to be sufficient to excite photoelectrons of all elements, but at the same time the natural line width of the x-ray transition should be narrow to obtain a high-energy resolution. Our XPS measurements are performed using a monochromatic Al $k\alpha$ source (1486.6 eV).

XPS has a choice between a monochromatic beam of a few microns in diameter or an unfocused non-monochromatic beam of a couple of centimeters. Due to the monochromatization only a small proportion of the total x-ray flux emission is selected. Therefore the resolution is higher when we use our monochromatic Al $k\alpha$ source. A disadvantage is that the photon flux available on the sample is much less than that in an unmonochromatized source [22, 23].

2.2.3 Analyzers

An electron energy analyser also called spectrometer measures electron velocities and converts it in a spectrum. A concentric hemispherical analyser (CHA) is often the used energy analyser and the basic set-up of a CHA is shown in Figure 7.B. CHA consist of two concentric hemispheres, the inner and outer one. The potential is different for both hemispheres and this will create a potential in the centre of the two hemispheres. This potential difference is varied so that photoelectrons of different kinetic energies can reach the detector. The slits in a CHA define the energy range that a photoelectron may have when entering or leaving the analyser. Photoelectrons that are of higher or lower kinetic energy are lost through collisions with the walls [23].

2.3 X-ray photoelectron spectroscopy

In XPS the sample surface is bombarded with photons from the x-ray source. The interaction between primary x-rays and the sample causes the ejection of core electrons from the atoms. The ejection of these photoelectrons is schematically represented in Figure 8 and it is the first signal that one can measure during the XPS analysis. The second signal is due to Auger electrons that may be emitted because the relaxation of the excited ions remaining after photoemission.

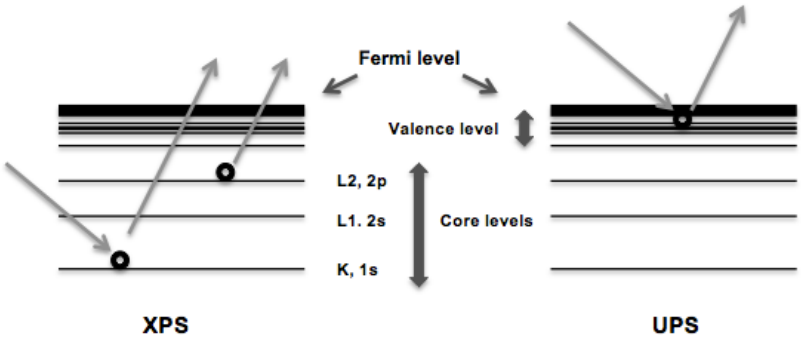

Figure 8: Energy diagram of photoemission process in ultraviolet photoelectron spectroscopy (right) compared to that of X-ray photoelectron spectroscopy (left).

During this process an outer electron falls into the inner orbital vacancy and a second electron is simultaneously emitted, carrying off the excess energy. The Auger electron effect occurs roughly 10^{-14} seconds after the photoelectric effect.

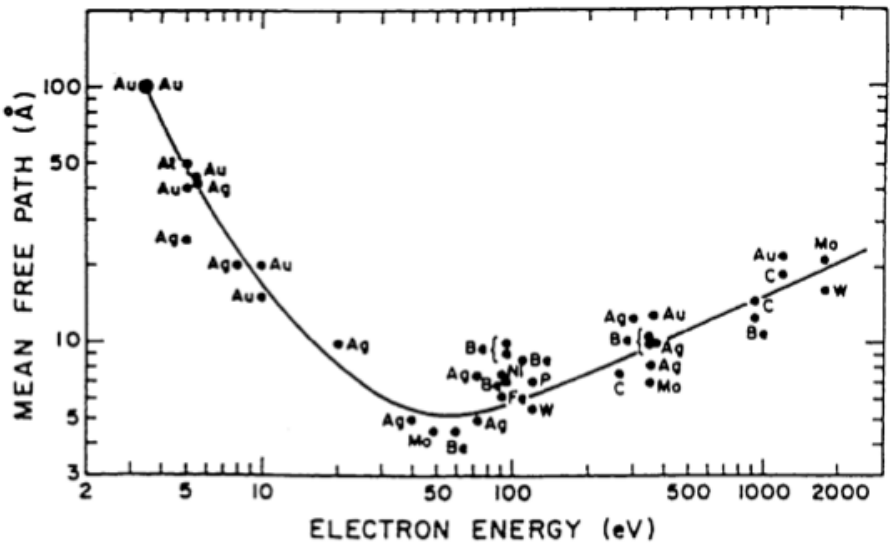

Figure 9: The "universal curve" for inelastic mean free paths, versus electron kinetic energy (eV) (23).

The x-ray photoelectron spectroscopy principle originates from the photoelectric effect, discovered by Hertz. If a photon with sufficient energy hits an electron in an atom the energy of the photon can be used to overcome the binding energy (*BE*) of the electron and emit it from the atom. The kinetic energy of the photoelectron (E_{kin}) can be calculated by the basic equation of XPS, Equation 2. The electrons are detected with an electron energy analyser, where they are filtered with an electric field. Therefore the work function ϕ of the electron analyser has to be considered as well as for the kinetic energy of the electrons.

$$E_{kin} = h\nu - BE - \phi$$

Equation 2: The basic formula for XPS, where *h* is the Planck constant and ν is the frequency of the incident photon, together the photonenery. *BE* represents the binding energy core level electron, E_{kin} the kinetic energy of ejected photoelectron and ϕ the work function.

As different elements have different core level binding energies, XPS can be used to identify different chemical species. The chemical surrounding can also be detected; they are visible in the spectra as chemical shifts. The XPS signal intensity is proportional to the amount of emitted electrons from a specific core level [(23)].

2.3.1 Surface sensitivity

The reason that XPS is a surface sensitive technique lies in the intense inelastic scattering that occurs for electrons in this energy range. If an electron travels through a medium it can undergo inelastic collisions with other electrons. During an inelastic collision the electrons will lose some of their kinetic energy. Due to this loss these electrons can only be detected at lower kinetic energies and therefore contribute to the background of the spectra. For an electron of intensity I_o emitted at a depth d below the surface, the intensity is attenuated according to the Beer-Lambert law. So, the intensity I_s of the same electron as it reaches the surface is given in Equation 3.
If the depth is three times the mean free path the signal is already reduced by 95%. Therefore quantity 3 λ is called information depth.

$$I_S = I_0 * e^{-d/\lambda}$$

Equation 3: Beer-Lambert law explaining the attenuation of the intensity due to inelastic collisions of the electrons in the sample. With I_0 representing the original intensity, I_s the measured intensity, d the travelled distance of the electrons ejected from the sample surface and λ the mean free path.

Thus λ is of great relevance in respect to the surface sensitivity of XPS. It mainly depends on the kinetic energy of the electrons, but also on the material. Figure 9 shows the so called "universal curve" for the dependence of the λ on the kinetic energy of the electrons. The curve has a minimum around 50-100 eV, so the best surface sensitivity is reached by bringing the kinetic energy of the electrons close to 100 eV [(23)].

2.4 Electron energy loss spectroscopy

Another important method for chemical analysis is electron energy loss spectroscopy. The technique measures electron loss events from a monochromatic electron beam after interaction with the sample. Vibrational motions of the atoms and molecules at the sample surface can be analysed by these energy losses. Therefore, EELS is used in material science to obtain structural, chemical and electronic information about a sample. Table 3 compares some important features of the used methods for surface analysis of samples in this thesis.

Table 3: Summarization of the basic factor for chemical surface analysis in UPS, XPS and EELS (23).

	Radiation detected	Input radiation	Information	Sensitivity	Quantification	Elements not covered
UPS	Electrons	Photon	Chemical	1%	Easy	N/A
EELS	Electrons	Electrons	Chemical	1%	Easy	N/A
XPS	Electrons	Photons	Chemical Elemental	0.3%	Easy	H, He

To start an EELS experiment, electrons from the source need to be accelerated to high energies (± 100 eV) before they enter the sample surface. Electrons are mostly scattered elastically, changing their direction but not their energy. However, a small part of the electrons is inelastically scattered. These inelastically scattered electrons lose energy to the sample due to specific excitations like, e.g., the creation of plasmons. EELS typically measures the distribution of inelastic scattered electrons with respect to the elastic peak

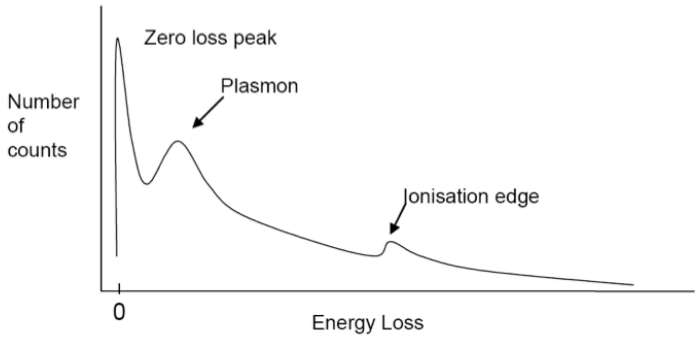

Figure 10: Basic graph of an EELS spectrum, showing the elemental features (zero loss peak, plasmon, ionization edge).

Figure 10 shows a schematic representation of an EELS spectrum. The largest signal occurs at energy loss zero, the zero loss peak (ZLP). This peak contains all electrons that crossed the sample without losing any energy. The energy loss spectrum of the inelastic scattered electrons is measured from this point on. Plasmon losses and ionization edges are the other principal features of such spectra [24, 25].

2.5 Atomic force microscopy

Atomic force microscopy is a scanning probe microscopy technique used to image the topography of structures with a resolution in the nanometer range. Microscopy imaging methods give information on the position and shape of the graphene flakes, but not on their surface morphology and height differences. These needs can be met by measuring the samples with AFM. Another advantage is that AFM allows imaging of both conductive and insulating samples.

The basic concept is that chemical forces, van der Waals forces and electrostatic forces act between a sample and a sharp tip. This sharp tip, which ideally consists of a single atom point, is scanned over the surface giving the x- and y-coordinates of the data. The determination of the z-coordinate depends on the chosen AFM mode but in principle all of them measure the force acting between tip and sample. The characteristic force distance curve is described by a Lennard-Jones potential and shown in Figure 11.A.

Two regions characterize this potential, they have a different potential gradient and there is a minimum between them. This leads to the development of two main AFM modes, contact mode and non-contact mode. All contact modes work on the branch with negative slope and the non-contact modes in the region with the positive one. The tapping mode combines both regions, working near the minimum of the potential. Non-contact mode is used for the AFM images of the graphene samples in this thesis [26, 27].

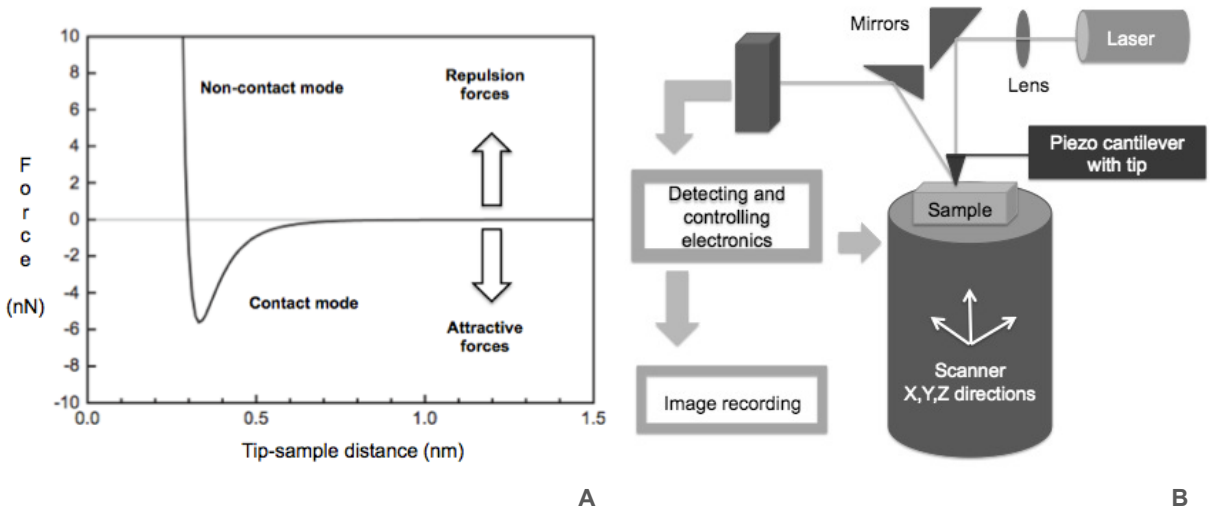

Figure 11: (A) The Lennard-Jones potential describes the acting forces (nN) between the tip and the sample in function of the distance (nm) between them. (B) A schematic illustration of an AFM set-up; the scanner moves the sample holder while the tip is at a fixed position. The force between the tip and the sample causes a deflection of the cantilever. These deflections are monitored by a photodetector and processed using imaging software.

The force between tip and sample surface is measured by the change in oscillation amplitude of the cantilever, whose bending is detected by the combination of a laser beam focused onto the cantilever backside and a position sensitive photodiode as shown in Figure 11.B. While the sample is scanned beneath the tip, a feedback loop adjusts the cantilever closer to or further away from the sample surface in order to keep the oscillation amplitude constant. The recorded information of the adjusted height values gives a topography image.

The lateral resolution depends on the tip size; a thinner tip gives a better resolution. Normally a resolution of 0.05 nm can be reached under ambient conditions. Other quantities can additionally be recorded such as the phase or the amplitude of the signal [26, 27].

The AFM used is a commercial ambient condition instrument Park systems NX10 and the AFM images were analysed and processed using the Gwyddion software.

2.6 Raman spectroscopy

Raman spectroscopy (RS) is an analytical method to obtain vibrational spectra of the molecules present in the sample. During the measurement the sample is radiated by a monochromatic laser beam of a certain wavelength λ and frequency. The monochromatic beam photons will interact with the sample and the light will be reflected, absorbed or scattered by the molecules present in the sample. The photons can be elastically scattered, without changing the λ or scattered by inelastic collision. RS detects the inelastic scattered signal. During inelastic scattering the photons will transfer energy, which will cause a slight difference in wavelength or frequency between the incoming and scattered light.

This phenomenon is called the Raman effect and it is illustrated in the Jablonski energy diagram, shown in Figure 12. The difference in frequency, the Stokes Raman shift, is due to transitions in the vibration states of the molecules [28, 29].

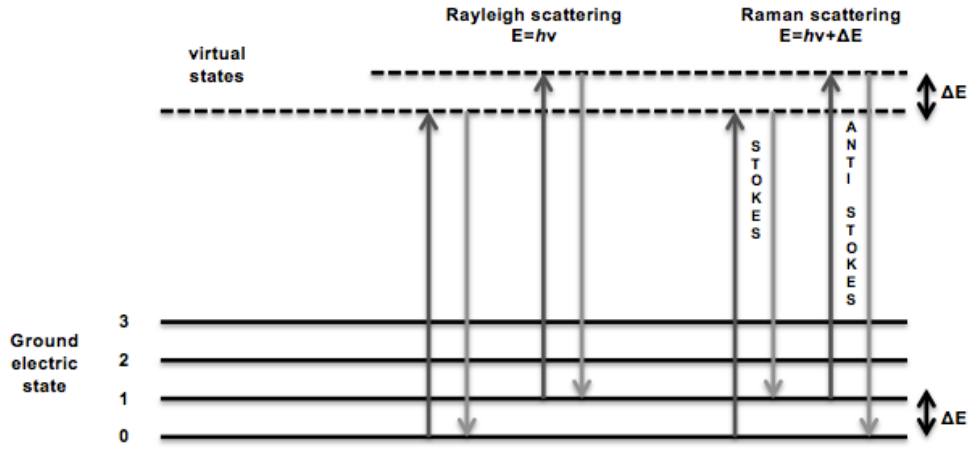

Figure 12: Jablonski energy diagram for Raman scattering. Irradiation by a laser will excite molecules from a vibrational state 1 or the ground state 0 to a higher energy level. Afterwards the molecules can fall back to lower energy states by either Rayleigh scattering or Raman scattering.

The monochromatic incoming light will thus result in variant wavelengths due to different Raman shifts. These different wavelengths are shown as Stokes Raman lines in the spectra and they represent the detected molecules. Raman shift due to lower frequencies are anti-Stokes lines, those due to higher frequencies are Stokes lines and Rayleigh lines still have the same frequency. An important condition for Raman scattering is that it can only be detected if there is a change in the electron distribution or polarization in a bond during vibration. Therefore molecules that have a centre of symmetry during the vibrations cannot be detected with RS [28, 29].

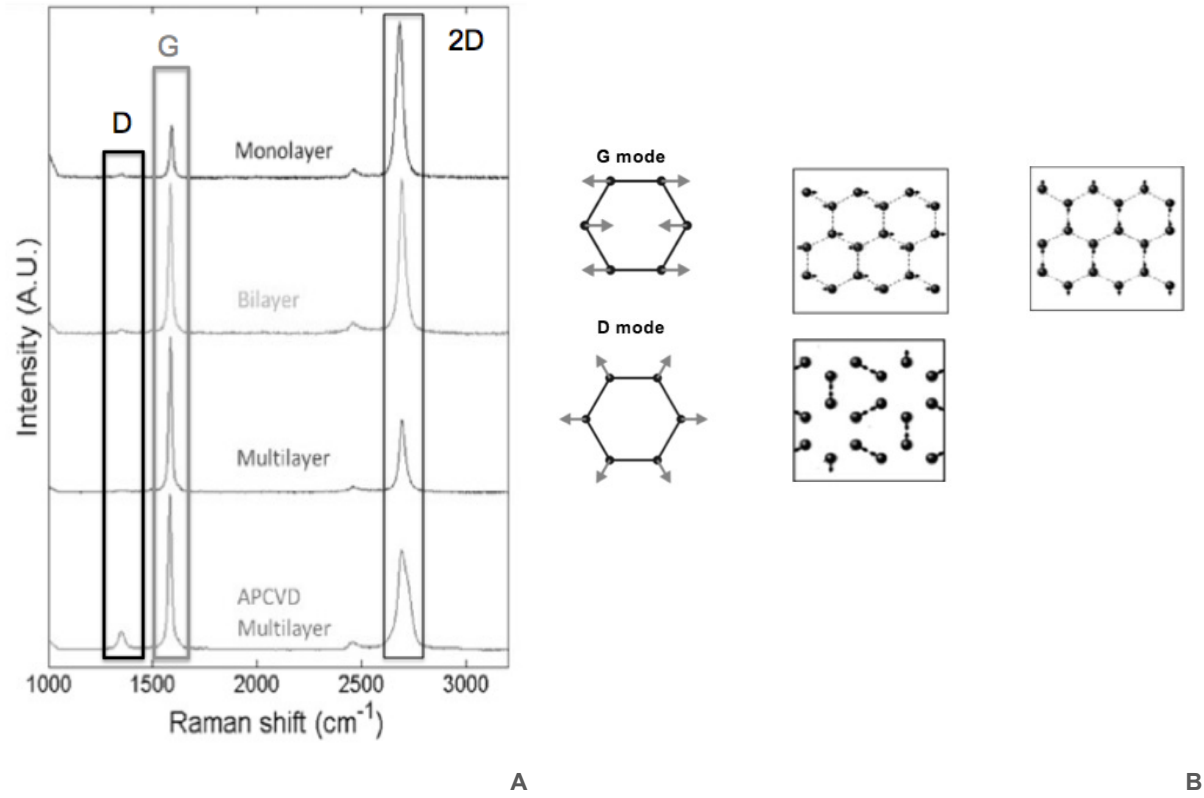

Figure 13: (A) Typical Raman spectra of single layer, multilayer graphene and graphite spectra with the 3 main features, a visible G and 2D peak and the small D band (9, 30). (B) Atomic displacements of the G and D mode (31).

Previous research has shown that RS is a powerful technique to identify the number of layers as well as the density of the defects of the graphene sample. In more advanced analysis it can also be used to determine the influence of strain, the local doping levels and for the study of the electrical properties or the electron-photon coupling effect.

Figure 13.A shows typical Raman spectra graphene and graphite with the most prominent features, the D peak, the G peak and the 2D peak. Graphite being composed out of multilayers of graphene shows similar Raman features. The G peak at 1580 cm^{-} and the 2D peak around 2700 cm^{-} are the main bands in the spectra. This is in contrast with the D band at 1355 cm^{-}. This peak is only present if there are unwanted carbon defects in the graphene layer (Figure 13.B). The presence of graphene can be determined by looking at the G band or G mode. It involves in plane bond stretching of the previous mentioned planar sp^2 bonded carbon atoms in graphene, see Figure 13.B.

The influence of the laser frequency is almost negligible on the position of the G peak, while the other bands shift with a change in laser energy. The other main peak in graphene spectra is the second order of D band, the 2D peak or G` peak. The 2D band shape and width provide information on the number of layers in the sample.
The ratio of intensity between the 2D peak and G peak (I_{2D}/I_G) is an important tool to discriminate single from multi-layered graphene. From Figure 13.A one can calculate that single layered graphene has an I_{2D}/I_G ratio larger than 2 and bilayer graphene has a ratio of 1. These are ideal values for the I_{2D}/I_G ratio; they can vary with the used laser frequency or energy. Another ratio that can be used to estimate the graphene layer quality is the I_D/I_G ratio. The I_D/I_G ratio is a measure of the disorder in the sample, which can be edges, charge puddles, ripples, or any other defect. A low I_D/I_G ratio indicates good quality graphene samples [31, 32].

The Raman measurements in this thesis were performed with T64000 Horiba scientific Raman system, using the 488 nm Argon laser. The 2D band intensity strongly depends on the laser energy. Costa et al. and previous research has shown that the I_{2D}/I_G decreases with an increasing laser energy or frequency. The highest 2D band intensities are reached using a 514 nm or 633 nm laser. Due to a higher laser energy the 2D band obtained in our spectra has a lower intensity and therefore we expect a lower I_{2D}/I_G ratio for our samples [33].

Chapter 3

Results and discussion

In this chapter the most important results of this thesis project are presented and discussed. An overview table of all the produced samples and their different CVD processes can be found in the appendix, Table 5. First, the Raman spectroscopy measurements of our graphene samples are analysed to estimate their quality. We will also discuss the morphology of our produced graphene by means of AFM images. Finally, XPS, EELS and UPS spectra are used to characterize the chemical composition of the graphene before/after exposure to 1 bar air and after the thermal treatment. Besides measuring our graphene samples, we also performed Raman, XPS and EELS measurements on a highly ordered pyrolytic graphite (HOPG) sample as reference.

3.1 Raman measurements

The Raman measurements of the graphene samples were performed using a polarized laser with a wavelength of 488 nm, under ambient conditions. Our used copper foils have a large backscattering signal, which will give a high background in the obtained spectra. In the next section, the most important data is presented and the rest of the Raman spectra can be found in the appendix Figures 35 to 46. First, a Raman spectrum of an annealed Cu sample is shown, as an example for the high background of the Cu samples. Then, Raman spectra of HOPG and our graphene on Cu samples are presented. Raman spectra of our graphene after the thermal treatment are also given in this first part. The second part contains an overview table of the two most important ratios I_{2D}/I_G and I_D/I_G of all the produced samples.

3.1.1 Raman spectra of annealed Cu, HOPG and graphene before and after treatment

Figure 14 shows the Raman spectrum of **an annealed copper sample**, magnification of the objective is x100. It displays the characteristic signatures of the influence of our Cu substrate in the obtained graphene Raman spectra. Copper will act as a mirror, providing a large backscattering signal and therefore a high noise level in the measurements. This sample was annealed for 40 minutes under 35 sccm hydrogen gas. In contrast to the HOPG sample and our graphene sample in Figures 15-18, the annealed Cu sample does not displays D, G or 2D peaks. This absence shows that there is no contamination in our reactor that could cause deposition of carbon structures

on our Cu substrates. Consequently, the carbon signals in the following Raman spectra are due to the addition of methane gas during the CVD processes.

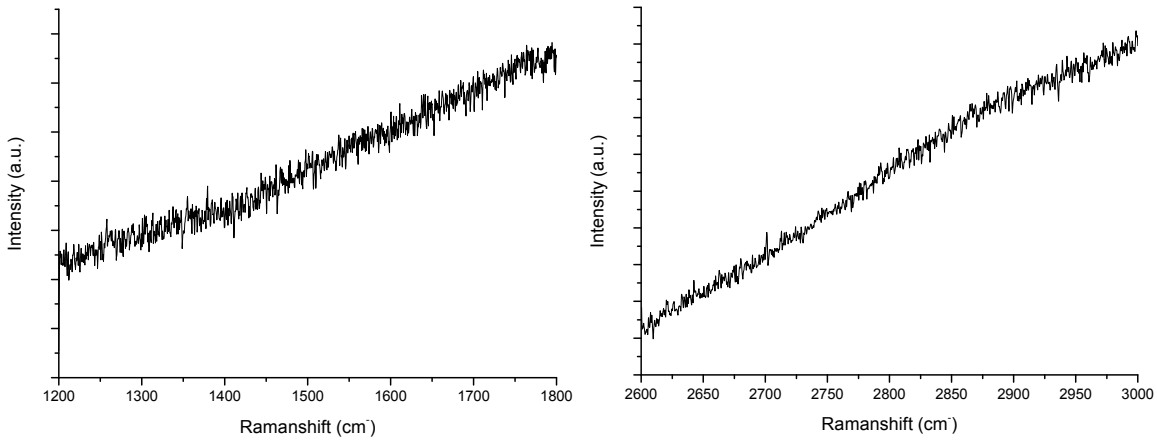

Figure 14: A typical Raman spectrum obtained from an annealed Cu foil (λ = 488 nm). There are no visible D, G or 2D bands present. Only the high background signal is visible in these spectra.

As mentioned previously **highly ordered pyrolytic graphite (HOPG)** and graphene exhibit only a few detectable Raman bands. A larger G peak observed at 1580 cm^-, due to C-C bond stretch vibration of the carbon atom lattice. The small and wide 2D peak at 2700 cm^- is also visible in the HOPG Raman spectra and the I_{2D}/I_G ratio is much lower than. The transformation of graphite to graphene leads to a decrease of the G band intensity. In addition the 2D peak shows a significant change in the shape and intensity.

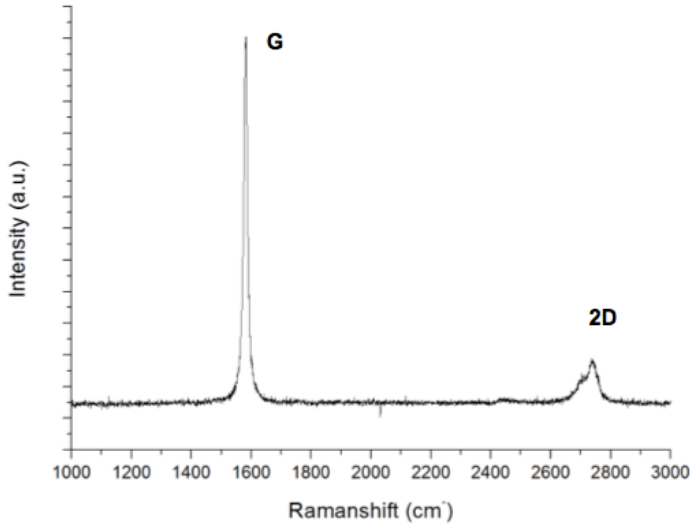

Figure 15: A typical Raman spectrum obtained from a HOPG sample (λ = 488 nm). These spectra show a strong G band at 1580 cm^- and a wide 2D band around 2700 cm^-. The Raman measurements are performed with the following parameters: objective magnification: x100; 3x120 s measuring time.

The following Figure 16 displays the characteristic signatures of **graphene** Raman spectra. Namely, the defect band or D peak at 1357 cm^-, which has a low intensity. This low signal is an indication that there are only a few defects in our graphene sample. The next bands are the G peak at 1580.9 cm^- and the 2D peak at 2711 cm^-.

The I_D/I_G and I_{2D}/I_G ratios of this graph are 0.069 and 1.38, these indicate that the graphene is of high quality, there is a low defect prevalence and that the number of graphene layers is between single layer I_{2D}/I_G (ratio lager as two) and a bilayer I_{2D}/I_G (ratio of one).

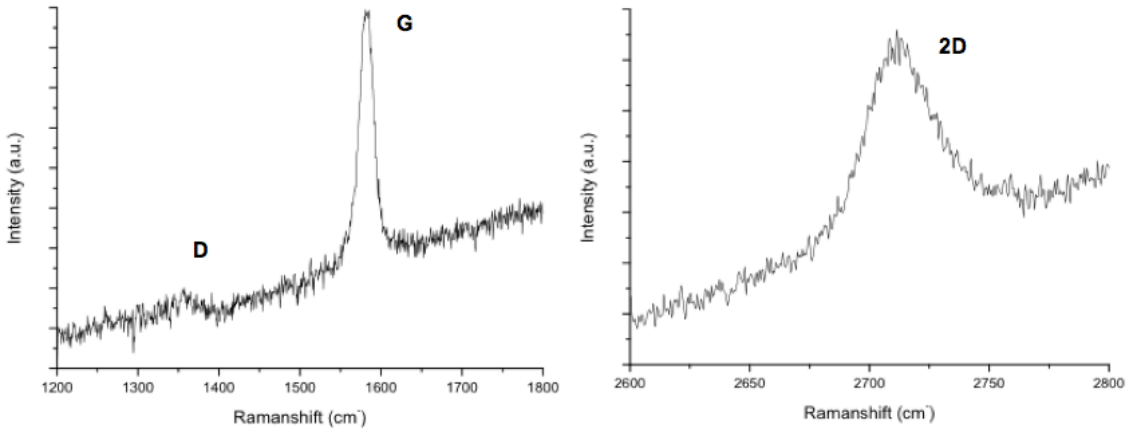

Figure 16: A typical Raman spectrum obtained from graphene (λ = 488nm). Small D (1357 cm$^-$) band contribution points towards a very low amount of defects. The high G peak (1580.9 cm$^-$) and 2D peak (2711 cm$^-$) indicate the formation of 1 to 2 layered graphene samples.

Figure 17 shows the Raman spectrum of the **graphene sample after thermal treatment** to remove the contamination due to exposure to 1 bar air. Despite their lower intensities, the G band at 1593.67 cm$^-$ and 2D band at 2694.32 cm$^-$ are still observed. The observation of the D peak at 1347.2 cm$^-$ is more prominent with a higher intensity.

When the ratios of the 2D and G peak intensities of the Raman spectra before and after treatments are compared, there is a decrease of a factor 2 visible. This, together with an increase in the D band intensity shows that the thermal treatment causes a small amount of damage in the graphene samples but the spectra are still recognizable. These Raman results will be compared to the XPS and EELS measurements in the next paragraphs.

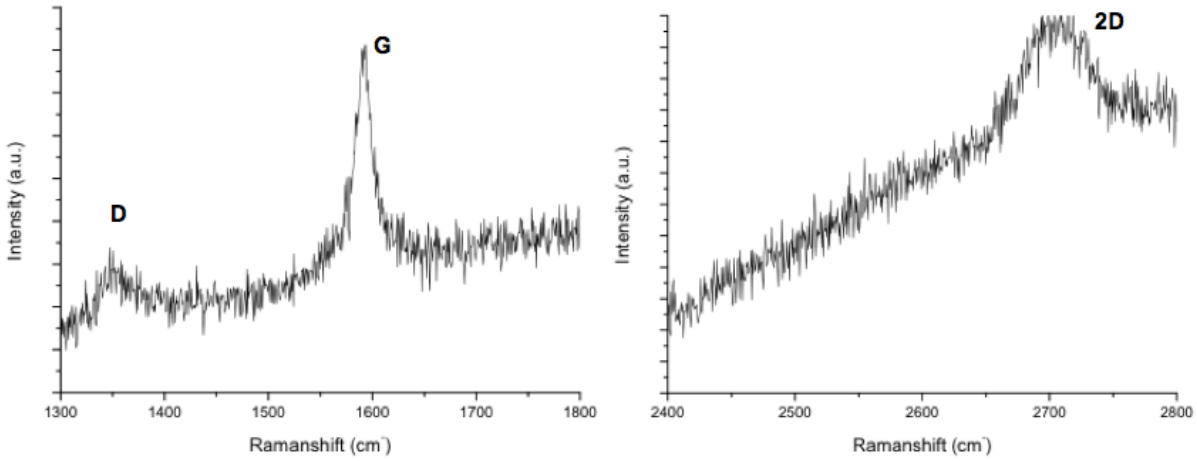

Figure 17: A Raman spectrum obtained from graphene after thermal treatment of 773 K and 973 K (λ = 488nm). The increased D (1347 cm$^-$) band points towards a small increase in the amount of defects. The high G peak (1593.6 cm$^-$) and 2D peak (2694.3 cm$^-$) indicate the formation of 1 to 2 layered graphene samples.

3.1.2 "Game changer" monolayer graphene on Cu

At the end of this thesis project, after having made some adaptations to the experimental set-up (heater system) in order to extend the stability of the deposition system at high temperature, monolayer graphene could be synthesized by increasing the CVD process time from 30 to 40 minutes. This is shown in Figure 18, which presents the characteristic signatures of **single layer graphene.**

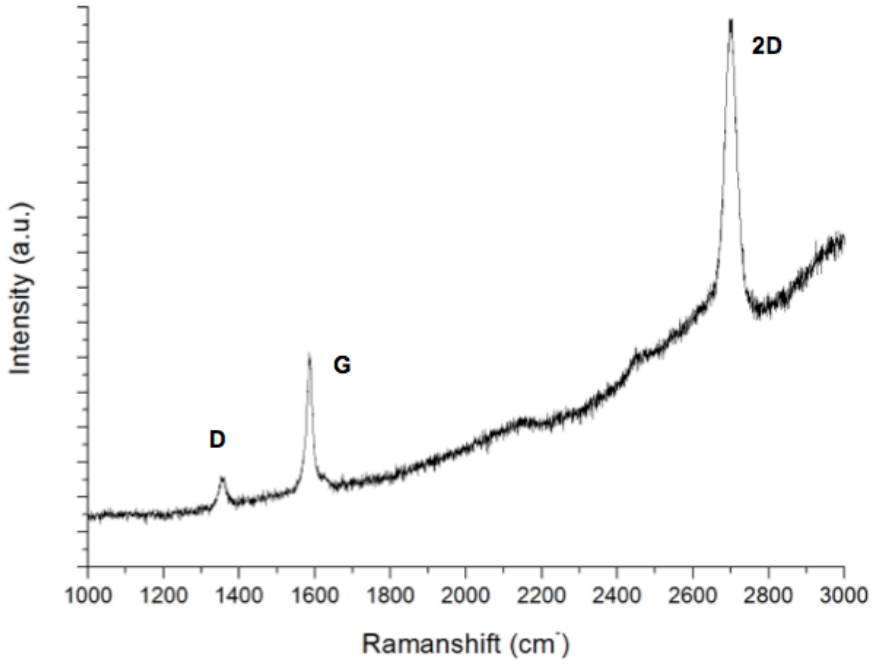

Figure 18: A Raman spectra of the produced single layer graphene (λ = 488nm) on copper. The D band at 1351.4 cm^{-} is rather small. While G band as well as a large 2D are located at 1584.7 cm^{-} and 2696.6 cm^{-}. The Raman measurements are performed with the following parameters: objective magnification: x100; 3x120 s measuring time.

The Raman spectrum shows a small defect band at 1351 cm^{-}. The G peak is located at 1584.7 cm^{-} and there is a large 2D peak visible at 2696.6 cm^{-}. The I_D/I_G and I_{2D}/I_G ratios of this graph are 0.18 and 2.17, proving that we produced single layer graphene of a reasonably quality.
Unfortunately, due to the time frame of the master thesis project, we did not have enough time to perform XPS, EELS our UPS measurements on this sample. However, chemical analysis of this sample and the underlying CVD process will definitely be explored in the very near future.

3.1.3 I_D/I_G and I_{2D}/I_G ratios table

The intensity ratio of the D/G band and 2D/G band are given in Table 4 and they will be used to estimate the amount of layers as well as the quality of our graphene samples. The Raman spectra of these values are all given in Figures 35 to 46, which can be found in the appendix. Due to the high background signal the intensities are calculated in Origin 8.0 after integration and the creation of a baseline for the different peaks.

The influence of the high background signal is clear when the intensities of the graphene samples 1 and 2 before and after their transfer to silicon dioxide (SiO_2) substrates are compared. Overall all the intensities increase, which is positive for the G and 2D band signal. The disadvantage is that this transfer causes more defects in the graphene structure, resulting in an increased D band intensity. Further elaboration of this transfer process could be a future prospect, but the transfer process is not discussed in this thesis.

The I_D/I_G ratio is used to measure the degree of disorder in the graphene lattice that arises from structural defects introduced during the CVD process as well as from the crystallite dimensions. The Tuinstra Köning relation in Equation 5 gives a formula to estimate graphene crystallite sizes (L_a) using Raman spectroscopy, where the value of the empirical constant C (E_{laser}) depends on laser energy [32, 34]:

$$\frac{I_D}{I_G} = \frac{C\,(E_{laser})}{L_a} \rightarrow L_a(nm) = \frac{(2.4*10^{-10})\lambda(488\,nm)^4}{I_D/I_G}$$

Equation 5: Tuinstra Köning relation to estimate the graphene crystallite size L_a (nm) using the I_D/I_G ratio and the laser excitation wavelength λ (nm).

Based on the above relation, we can conclude that the CVD process used for sample 5 creates the best quality bilayer graphene sheets. The graphene of sample 5 shows ordered graphitic regions with a size of ~197 nm surrounded by areas of carbon defects or edges. This value can be directly compared with the size of the areas observed in the AFM images, reported in the next section. When we look at the single layer graphene flakes in sample 12 we see a larger I_D/I_G ratio and consequently their diameter will be smaller, approximately 75 nm.

Table 4: Overview table of the intensity ratio of the D/G band and 2D/G band of the different samples and their CVD processes. The symbol X indicates that the intensity of the peak was not significantly higher as the background signal and therefore could not be integrated in our calculations.

Samples	I_D/I_G ratio	I_{2D}/I_G ratio	Samples	I_D/I_G ratio	I_{2D}/I_G ratio
Sample 1 on Cu	X	X	**Sample 6 annealed Cu**	X	X
Sample 1 on Si	1.47	0.40	**Sample 7 on Cu**	0.22	0.21
Sample 2 on Cu	0.44	X	**Sample 8 on Cu**	0.44	1.05
Sample 3 on Si	0.20	0.36	**Sample 9 on Cu**	0.08	X
Sample 4 on Cu	0.41	1.31	**Sample 12 on Cu**	0.18	2.13
Sample 5 on Cu	0.069	1.38	**HOPG sample**	X	0.16
Sample 5 after treatment	0.28	0.71			

High quality single layer graphene has a sharp 2D peak, roughly at least twice the intensity of the G peak. An increase of the amount of layers in the graphene sample will lead to significant decrease in intensity of the 2D band. Bilayer graphene therefore has a large band or a larger FWHM as single layer graphene and the I_{2D}/I_G ratio is decreased. Graphene samples with more than five layers have Raman spectra that are almost identical to that of bulk graphite (HOPG).

Thus, with the use of Raman spectroscopy one can clearly distinguish a single layer, from bi-layer or multi-layer by looking at the 2D/G band ratio. Again when we look at the calculated ratio in Table 4, sample 12 has the highest I_{2D}/I_G ratio value and therefore the best suited CVD process to produce single layer graphene. The bilayer graphene in sample 5 is also of good quality, thus allowing to study its chemical and electronic properties using XPS, EELS and UPS as presented below.

3.2 Optical and AFM images

As previously mentioned, it is still a challenge to produce large area uniform graphene sheets suitable for applications. CVD on Cu has proven to be a practical solution for low defect graphene with a controlled synthesis. During our CVD processes methane was decomposed on Cu foil at high temperature. Due to the limited solubility of carbon in Cu, CVD on Cu substrates results in mono- or bilayer graphene sheets with dimensions up to several inches. Obviously, the unpolished surface of these polycrystalline Cu foils is very different from single-crystalline Cu (111) substrates and the graphene growth should be strongly influenced by the presence of a polycrystalline surface. To gain more control over the production process of graphene, it is of major importance to understand the interaction between our grown graphene sheet and such Cu foils.
Hence, some AFM results of as-grown graphene layers on Cu are presented below. These AFM images are used to study the continuity of the graphene on top of the Cu foil.

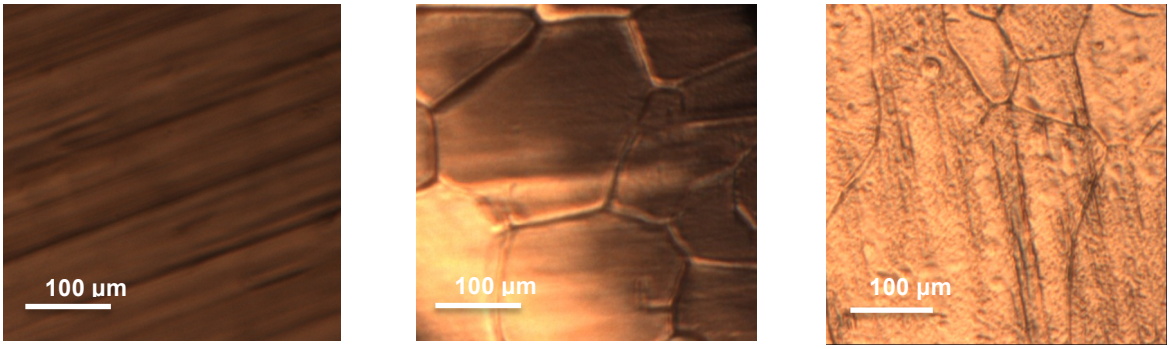

Figure 19: Optical microscope images of untreated Cu foil (left), annealed Cu (middle) and graphene on Cu (right). Thermal annealing under UHV conditions will make the Cu foils more crystalline.

Y. Zhang et al. and L Zhao et al. have shown that graphene domains can span over several micrometers and the domain orientation does not depend on the Cu substrate symmetry [7, 8, 35, 36]. Figure 19 shows optical microscope images of the copper foil morphology before CVD and after different CVD steps. There is a clear difference visible between the untreated Cu substrate (left side) and after its annealing to the deposition temperature (the middle image, no growth yet). Microscopic structures ('flakes') appear after heat treatment, indicating the thermal behavior of our polycrystalline Cu foils. Y. Zhang et al. also shown that this thermal behavior of Cu is very distinct from that of graphene and that the formation of wrinkles and ripples is related to this difference [36]. The higher thermal expansion coefficients of Cu result in more contraction between the Cu surface and the graphene, leading to the release of graphene on certain places and so the formation of wrinkles.
In the next figures the most important AFM images and their height profiles are selected, to explain the correlation between the Cu surface and the grown graphene sheets.

Figure 20 illustrates the topography of an **annealed Cu foil**, which was heated for 40 minutes at 390 Watt with a flow rate of 50 sccm hydrogen gas. The 2D and 3D AFM images show lamellar structures caused by the high temperature. From the line profile the height differences between the different lamellas or terraces, which can be determined yielding an average step height of ~8 nm and a width of 100 nm. The absence of height variations within the terraces (due to wrinkles) together with the previous Raman results indicate that there is no graphene present on the Cu substrate yet despite the presence of carbon-based residual gas molecules (like CO) during annealing under UHV conditions.

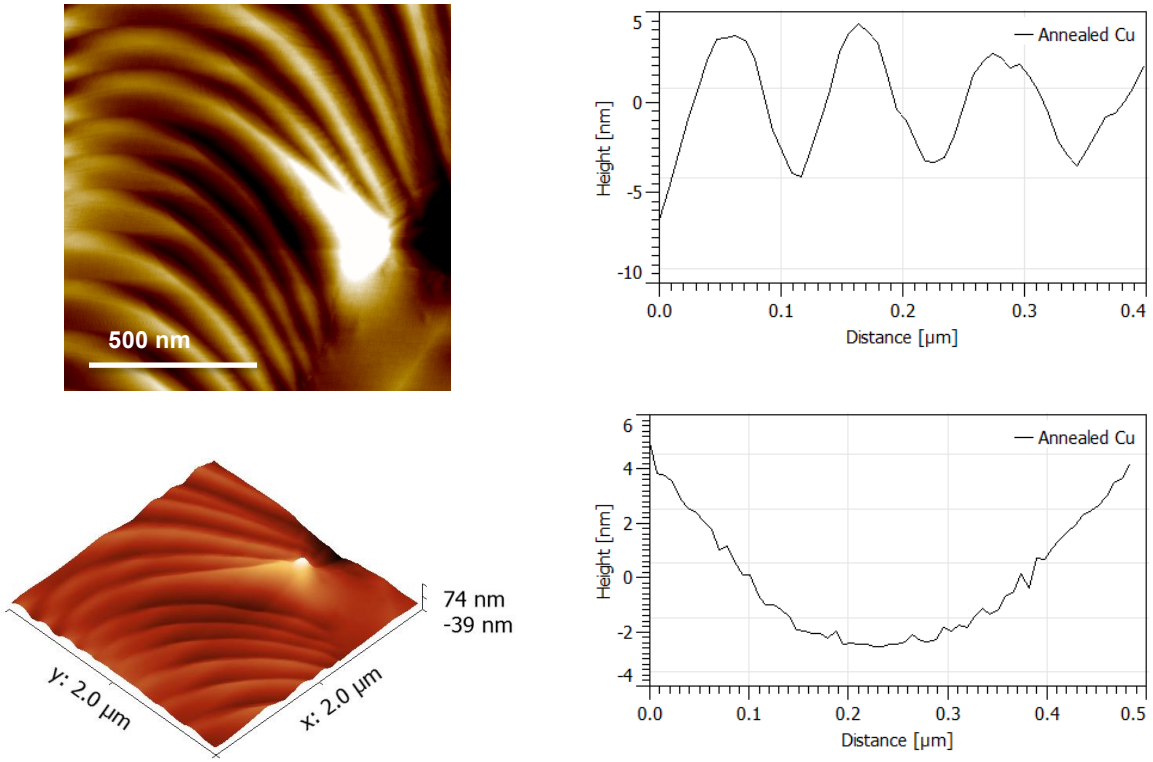

Figure 20: AFM topography image of an annealed Cu foil sample 6 (upper left picture). The Cu foil was heated for 40 min at 390 Watt under 50 sccm of hydrogen gas. A 3D (lower left picture) close-up image demonstrating clear lattice distortions and corresponding section views across the different planes (upper line profile) and in plane (lower line profile) are presented on the right side. These height profiles show that the big steps (visible lammeala on the 3D image) are around 10 nm, while the height inside one plane does not show any significant height differences.

There are clear morphological differences visible when comparing Figure 20 (annealed Cu) with Figures 21 or 23, both representing **graphene on Cu**. Figure 21 depicts an AFM image taken on sample 4. Here, the produced graphene is of lower quality than that of sample 5 shown in Figure 23. Raman spectra of sample 4 show a higher I_D/I_G ratio, which indicates the presence of more carbon defects. Our 2D and 3D AFM images show the presence of undesired Cu_xO nanodots. From the dark planes in the phase image it is clear that there is still uncovered Cu present. Wen Ge et al. have shown that these not fully covered Cu surfaces result in the formation of nanodots at the edges [8].

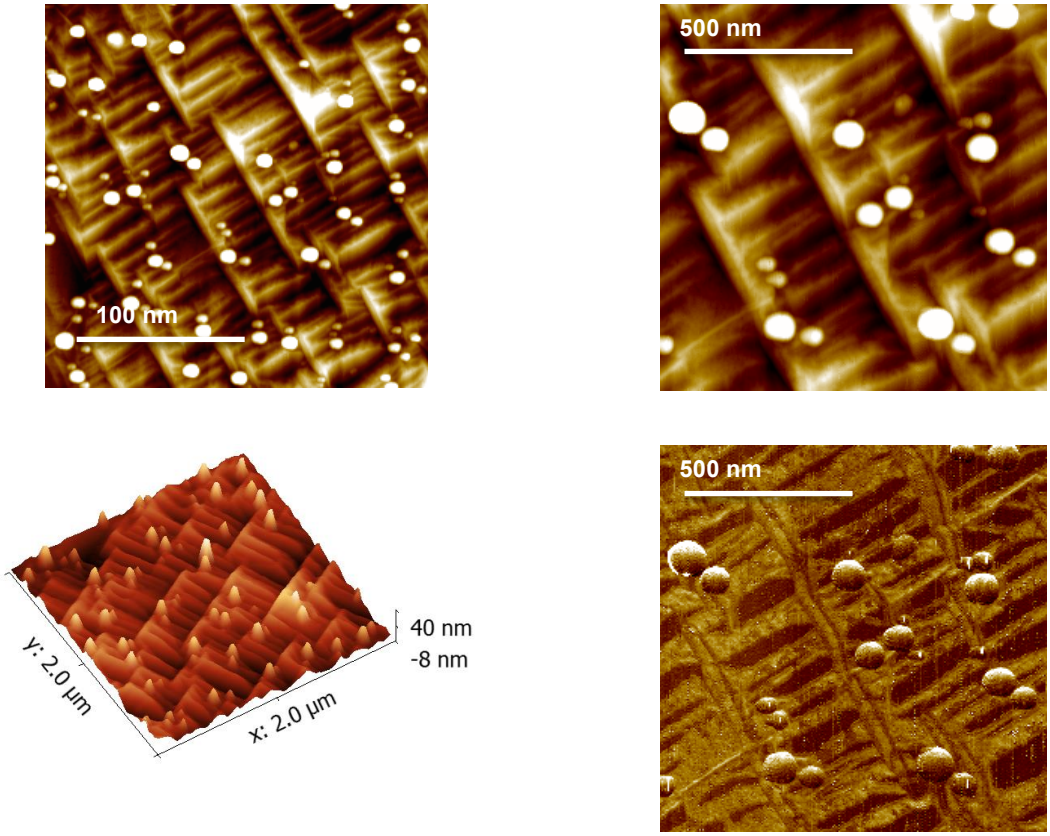

Figure 21: AFM topography 2D and 3D images of sample 4. The CVD process can be found in the appendix. There are a lot of copper oxide nanodots present. From the phase image (lower right picture) the non-covered Cu is visible as the darker parts while the graphene layer is indicated by the lighter colour.

A series of AFM images of graphene on Cu are shown in Figure 22. On these pictures graphene flakes on Cu terraces are indicated and their boundaries are clearly visible. These Cu terraces provide good graphene nucleation sites, this effect will be explained in Figure 22.

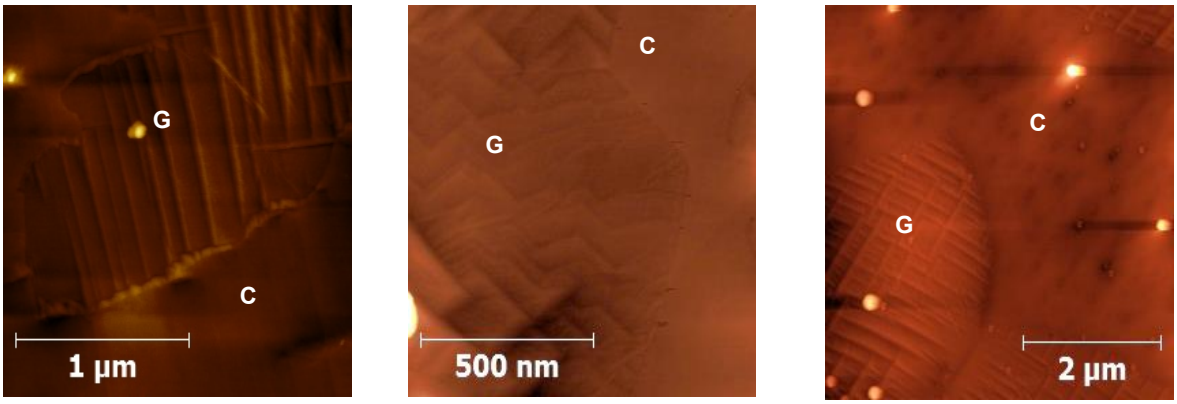

Figure 22: AFM images of graphene on copper samples where the graphene domain boundaries are clearly visible. Graphene and Cu are indicated as "G" and "C" respectively.

The presence of the nanodots is almost negligible in the AFM image of sample 5 presented in Figure 23. In this figure carbon lattices on terraced regions can be observed. Again the terrace steps are around 8 nm in height over 100 nm distance, but besides this observation there are also in plane height differences. In contrast to Figure 20, this line profile (lower line profile on the right) show height difference between 0.5 and 0.8 nm in plane.
Zhang et al. confirm that these findings in height differences can indicate the presence of wrinkles or ripples over an average of 30 nm. These AFM images together with the previously shown Raman spectra prove that we were able to produce graphene sheets on our copper substrate terraces [36].

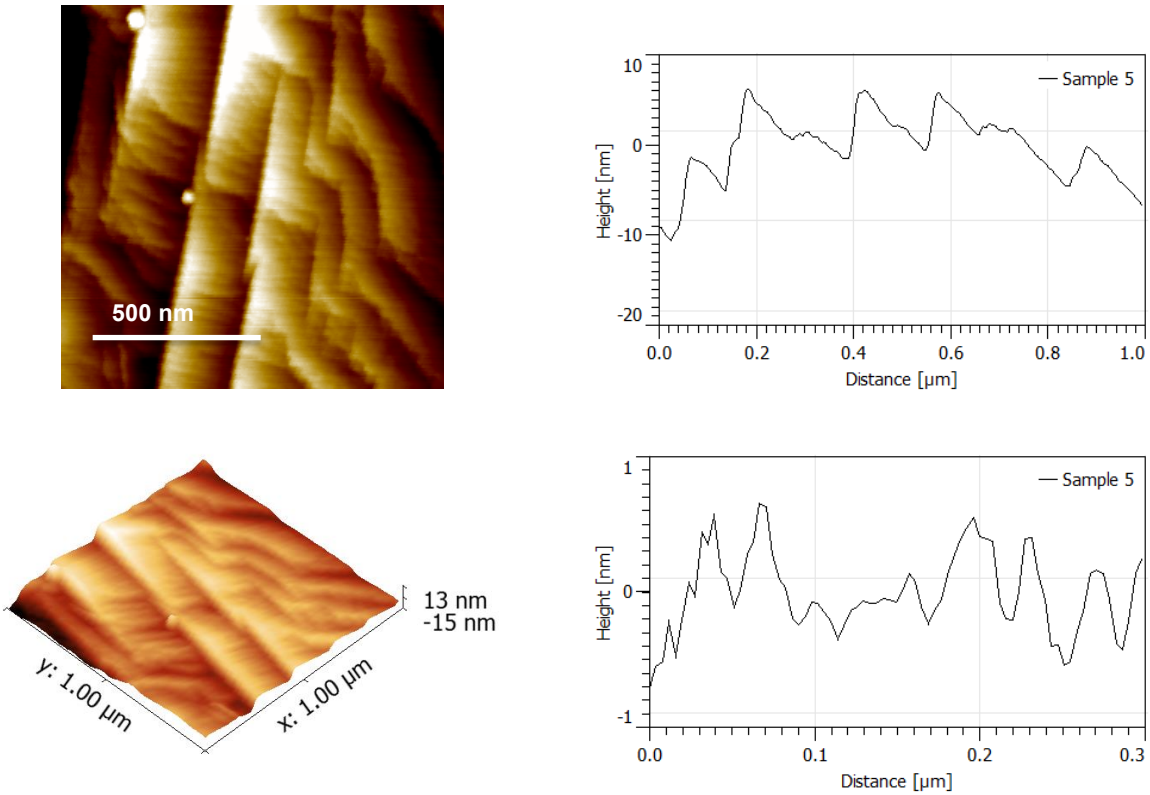

Figure 23: AFM topography 2D and 3D images of sample 5 (left). The CVD process can be found in the appendix. There are almost no copper oxide nanodots present. Corresponding section views across the different teraces (upper line profile) and in plane of a terace step (lower line profile) are presented on the right side. These height profiles show that the big steps are around 8 nm, while the height inside one plane changes with 0.5 to 0.8 nm.

So far, this work indicates that we have grown bilayer graphene flakes with diameters of around 197 nm diameter. Overall there are only weak interactions between the graphene and the copper substrate. But due to thermal expansion defect ripples and wrinkles can evolve along areas where there is strain release. Furthermore, this strain effect due to the perfect two-dimensional graphene that lies on the highly polycrystalline Cu surface is found to induce local bonding between the graphene sheet and its substrate. This will cause configuration changes of the carbon atoms from sp^2 to sp^3 hybridization [36].

3.3 XPS, EELS and UPS analysis

XPS, EELS and UPS are all surface sensitive spectroscopy methods, which make them ideal candidates to study one atom thick graphene sheets. By measuring our graphene samples in situ after CVD, we eliminate the presence of surface contaminations. These in situ measurements will be compared with post growth measurements, after exposing our samples to ambient conditions. These results will determine the graphene-Cu interaction after growth as well as the influence of an ambient environment on the chemical character of graphene. We also aim on finding a treatment to remove these air-based contaminations. Therefore, we subject our exposed graphene sample to two thermal treatments. The results of these thermal treatments are also analysed with XPS and EELS. Beside graphene samples chemical analysis was also performed on a HOPG sample serving as a reference.
Most of the spectra have a background signal. This background is subtracted during peak analysis in Origin to obtain correct intensity values.

3.3.1 Survey XPS measurement of Cu substrate before and after treatment

Before starting with the CVD process of graphene, we measured the Cu foil 99.999% of Alfa Aesar that will serve as substrate and catalyst. A wide XPS scan was performed before and after the annealing step. During the annealing step the Cu foil was heated for 20 minutes at 1200 K under a continuous flow of 35 sccm H_2 gas.

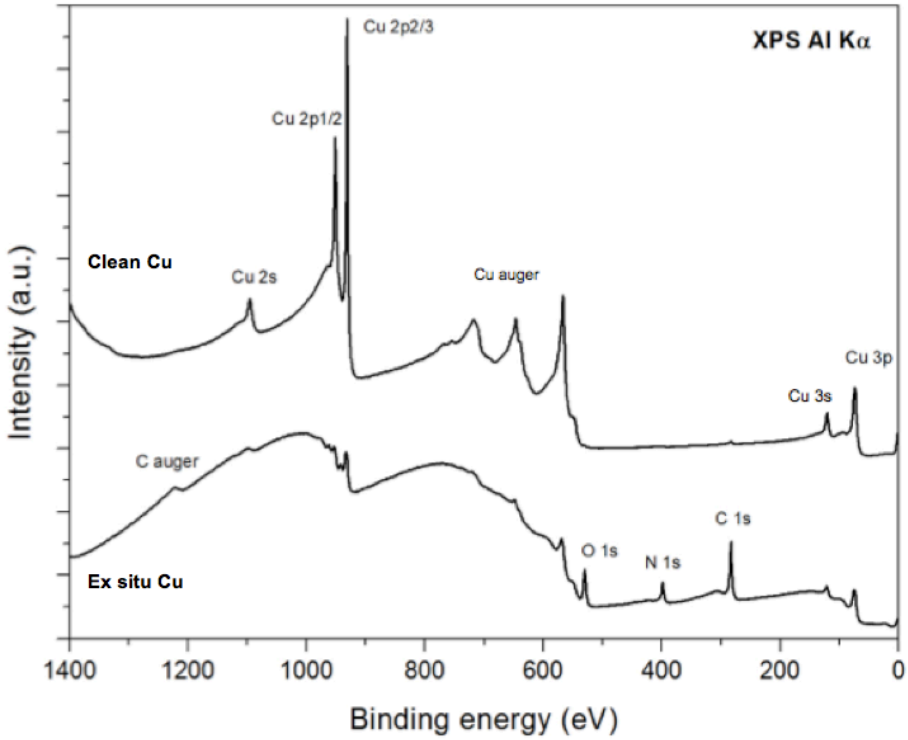

Figure 24: Wide scans of a contaminated (ex situ) Cu foil before (bottom curve) and after (top curve) its in situ cleaning. The major Cu peaks arising from the clean sample are the most intensive ones. On the contaminated sample the presence of C, N and O surface impurities is visible. These survey scans were recorded at a pass energy of 187 eV.

Figure 24 displays the two wide XPS spectra of annealed Cu and untreated Cu. All the intensive peaks of the clean Cu surface are almost completely damped by contaminations from exposure to air. The major elements in this contamination layer that covers the Cu foil are due to hydrocarbon peaks (C 1s peak at 284.5 eV), oxygen (O 1s around 533 eV) and nitrogen (N 1s at 400 eV). After the annealing step, all these contaminations are removed and a clean Cu surface remains. This clean surface will serve as catalyst during the subsequent growth of graphene by CVD.

3.3.2 XPS survey of Graphene on Cu and HOPG

When a wide XPS scan of graphene on Cu substrate is compared to that of HOPG, there are clear differences (Figure 25). The XPS survey of HOPG only shows carbon peaks, a very large C 1s peak and a small C auger peak around 484 eV and 1221 eV, respectively. In contrast, the major peaks in the graphene/Cu spectrum are caused by photoemission from the underlying Cu substrate. As expected, a small C 1s peak appeared after the growth step. This small peak indicates that there is formation of carbon deposits on the Cu foil. Raman and AFM images confirm that this carbon peak is due to the formation of bilayer graphene on the Cu foil.

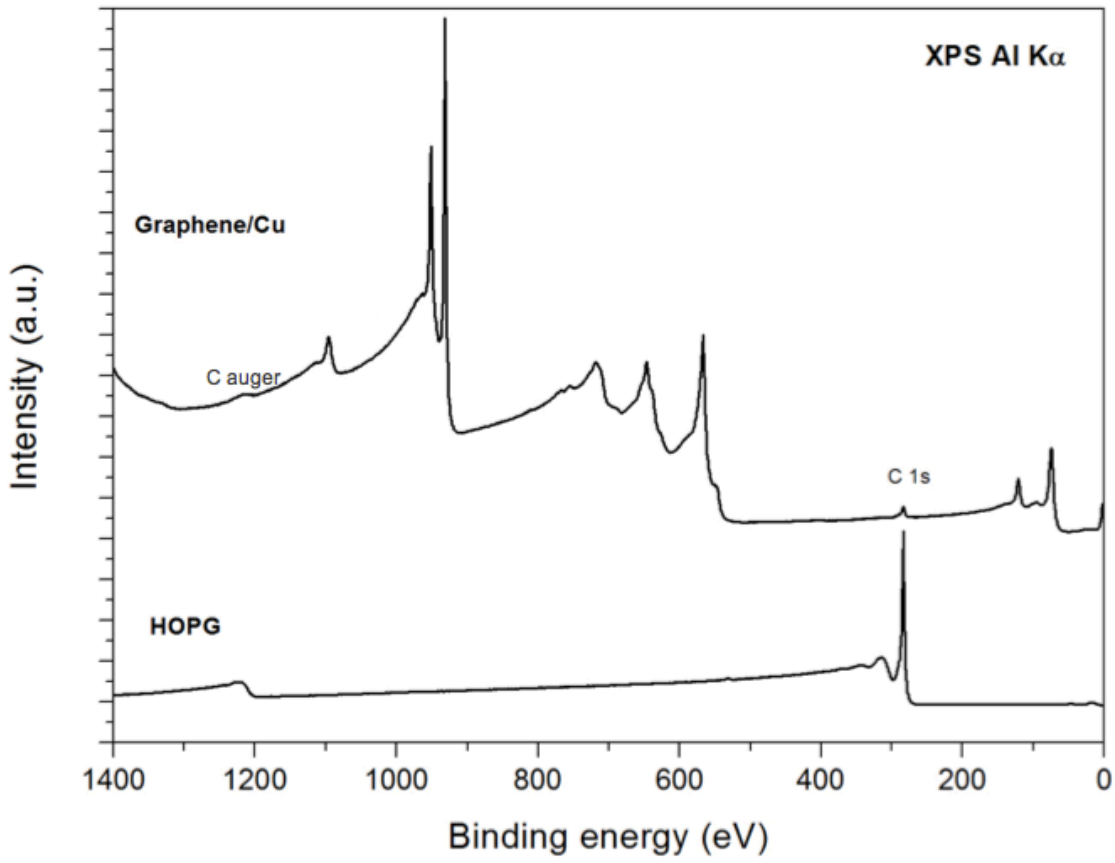

Figure 25: Wide scan of a graphene/Cu sample and HOPG serving as reference. The major Cu peaks arising from the Cu substrate are still the most intensive ones, but there also appears a small C 1s peak (284.5 eV). This C 1s peak has a much higher intensity in the HOPG graph. These surveys were recorded at pass energy of 187 eV.

3.3.3 XPS survey of annealed Cu, graphene on Cu and graphene after exposure

The wide XPS scans in Figure 26 compare an annealed Cu foil and graphene on Cu sample before and after exposure to 1 bar air. It illustrates the change in the carbon 1s, oxygen 1s and Cu $2p_{2/3}$ peaks.
The carbon 1s peak appears after the growth step during the CVD process and its intensity increases after air exposure. This increase is caused by the absorption of hydrocarbons form the air on the graphene sample. Exposure to air also causes oxygen contaminations and the Cu peak intensity decreases due to large damping effect caused by the contamination layers on top of the Cu substrate.

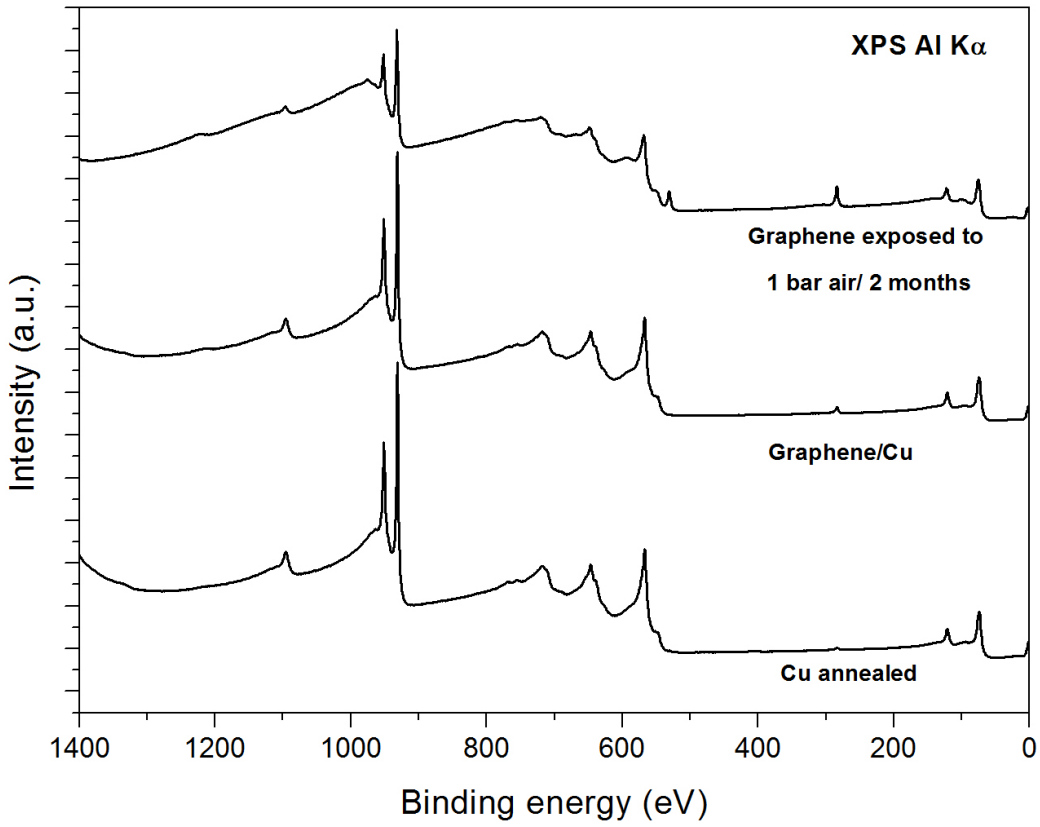

Figure 26: Wide scans of an annealed Cu sample and a graphene on Cu sample before and after exposure to 1 bar air. The major Cu peaks arising from the Cu substrate are still the most intensive ones in all the spectra, but there also appeared a small C 1s peak (284.5 eV). This C 1s peak has a large intensity after air exposure due to hydrocarbon absorption. After air exposure there is also an O 1s peak present (533 eV). These survey scans were recorded at a pass energy of 187 eV.

The overview scans presented in Figure 26 give a first impression of the changes induced during the CVD process and after exposure to air for an extended time. They show that all contaminations can be removed from the Cu foil by heating it at 1200 K for 20 min under a continued flow of 35 sccm. After this annealing step graphene growth can start, the formation of graphene will give rise to a small C 1s signal and a very small damping effect that decreases the Cu 2p doublet. After their exposure to air, graphene/Cu samples reveal the presence of contaminations on the sample surface. Absorption of hydrocarbon and oxygen is detected as well as a larger damping effect of the Cu signal. The following XPS measurements analyse changes in the Cu $2p_{2/3}$, C 1s and O 1s peaks in more detail, damping effects are calculated and chemical shifts are analysed.

3.3.4 XPS measurement of C 1s peaks of HOPG, graphene on Cu before/after exposure and treatment

Figure 27 shows the evolution of the C 1s XPS spectra of graphene after CVD, air exposure and thermal treatment. As previously shown, there were no carbon signals present after the annealing of the Cu substrate under hydrogen atmosphere in UHV (XPS survey shown in Figure 26). Upon methane exposure a carbon peak component appeared around 284.7 eV in our graphene on copper sample (graphene/Cu). Other XPS spectra obtained after exposure to air or after thermal treatment show two different carbon components located at binding energies of 284.4 eV and 285.2 eV. Differences in the defect density and graphene copper interaction cause this variation of main carbon positions.

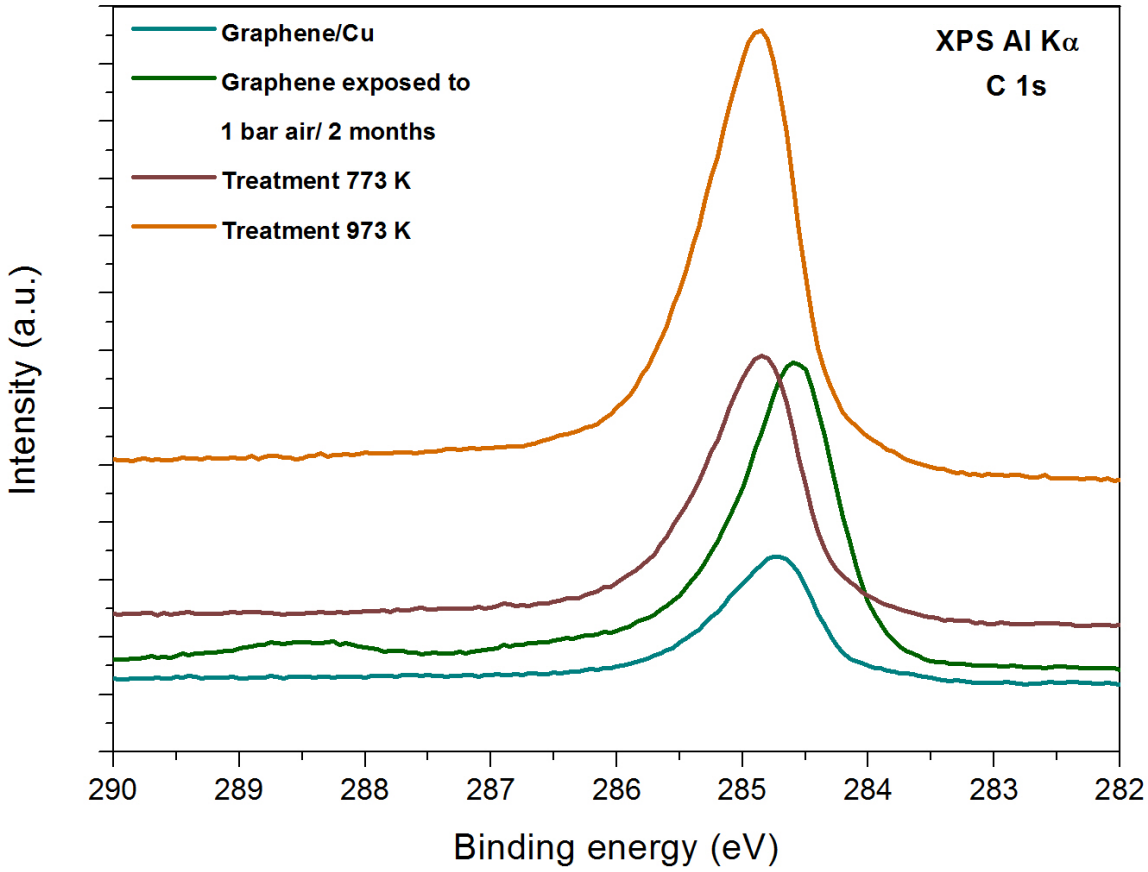

Sample	Position	Sample/position	Position
Graphene/Cu	284.75 eV	**Treatment 773 K**	284.85 eV
Graphene exposed to 1 bar air/2 months	284.6 eV	**Treatment 973 K**	284.85 eV

Figure 27: Overview of the C 1s peaks of a graphene on Cu sample (graphene/Cu), a graphene on copper sample after 2 months of air exposure and a graphene sample after the two thermal treatments. The table under the graph shows the position of the carbon peaks maximum. These max positions may not be confused with the carbon components, which are located in the different carbon peaks. These spectra were recorded at pass energy 6 eV.

The observed C1s position in the graphene/Cu sample is consistent with findings of Kidambi P. et al. [9]. When this value is compared to that of HOPG (Figure 28), given in Figure 28, we see some clear differences in the binding energy. The main carbon component is at 284.4 eV for HOPG, while that of graphene on Cu is positioned at a higher binding energy (284.7 eV) thus, indicating an interaction between the substrate and the graphene layer. The higher binding energy is due to interactions between the Cu substrate and graphene, which eventually causes a charge transfer between the two sub-systems (Kidambi P. et al.). When we look at the XPS spectrum of our graphene samples after they have been exposed to air for two months, we see a small shift towards a lower binding energy (Figure 27). This might reflect a modification in the interaction between the graphene and its Cu substrate due to adsorbates/chemisorbates from the ambient.

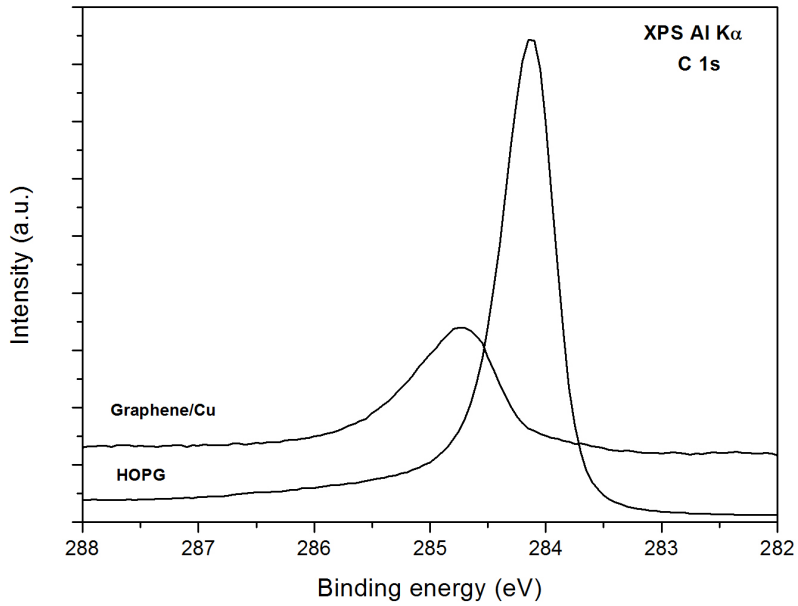

Figure 28: High-resolution XPS spectra of the C 1s core level region of our graphene on copper sample and a HOPG sample serving as reference. The C 1s peak is located at 284.75 eV for the graphene sample and at 284.2 eV for the HOPG sample. These spectra were recorded at a pass energy 6 eV.

Beside a shift of the main C 1s line, the XPS spectrum in Figure 29 reveals two additional components caused by the interaction of carbon atoms with oxygen-related species. The first component around 286.5 eV is assigned to alcohol (C-OH) groups, the second around 288.7 eV arises from carbonyl (O-C=O) groups, thus reflecting the presence of complex surface contaminations with strong polar character. After the thermal treatments a shift back towards the position of the in situ prepared graphene can be seen accompanied by the disappearance of the carboxyl contamination thus indicating a cleaning effect due to annealing.

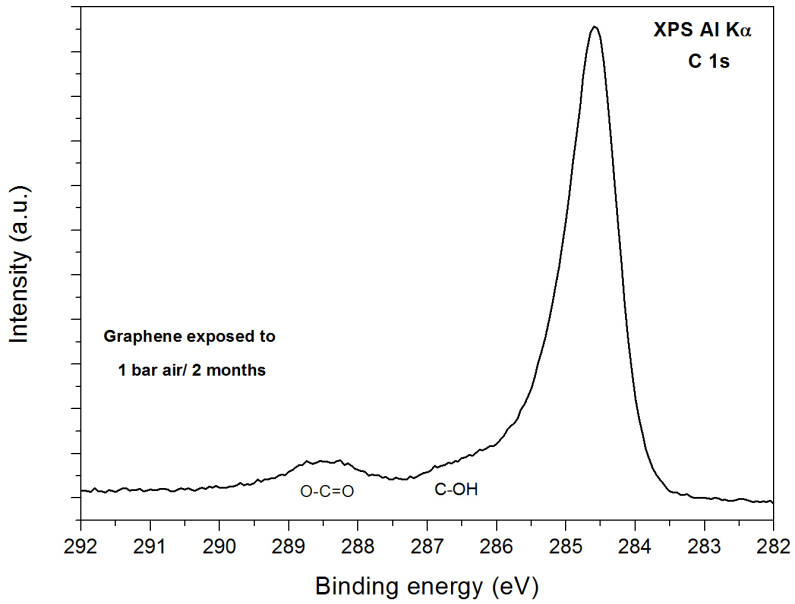

Figure 29: XPS data of a graphene on copper sample after it has been exposed to air for two months. The C 1s core region with its maximum at 284.6 eV shows the presence of three components. The first peak around 286.5 eV is assigned to alcohol (C-OH) groups, the second around 287.5 eV is caused by C=O groups and the third rises from the carbonyl (O-C=O) groups around 288.7 eV. This spectrum was recorded at pass energy 6 eV.

Overall we conclude that the main C1s component represents graphene on Cu, while the additional contributions reflect an interaction of the graphene layer with different physisorbed/chemisorbed oxygen species. As already mentioned in the AFM results, graphene will only occasionally form weak bonds with the copper substrate, causing the formation of wrinkles or ripples. These weak interactions with the substrate will break due to absorption/intercalation of oxygen-related polar species when our graphene samples are exposed to air. After appropriate heat treatments we see the removal of carbonyl and alcohol groups. This is a first indication that our thermal treatments are sufficient in removing the absorbed oxygen and in restoring the copper graphene interactions.

3.3.5 XPS characterization of Cu peak on annealed Cu and graphene on Cu

In addition to this detailed chemical analysis of the carbon component, in situ high-resolution XPS studies are also performed on the Cu $2p_{2/3}$ core level. Figure 30 shows two XPS spectra of this copper peak located at 932.7 eV, one spectrum acquired after the hydrogen annealing step and the other one after exposure to methane gas during the growth process.

When we look at the spectra there is a difference, which is due to the damping effect of the carbon layer on the copper signal. In the simple case of a homogeneous graphene layer on a copper substrate the layer thickness (d) can be calculated by the damping effect given in Equation 6 [23, 37].

$$d = -\ln\left(\frac{I_{Cu\,(d)}}{I_{Cu\,(0)}}\right)\lambda_C \cos(\theta)$$

Equation 6: Formula used to calculate the graphene layer thickness by using the intensity of the copper peak before and after graphene growth ($I_{Cu(0)}$ and $I_{Cu(d)}$) the mean free path of carbon λ_C and the emission angle θ (during our measurement this angle was set at 20 degrees).

This formula estimates the thickness of the formed graphene layer to be around 0.3 nm by using the inelastic mean free path of carbon, the emission angle of the photoelectrons and the measured photoemission intensities of Cu before and after growth. One carbon layer is estimated to have a thickness of 0.22 nm, this calculation thus agrees well with the information derived from the I_{2D}/I_G ratio of our Raman measurements (Figure 16) which pointed towards a bilayer graphene on our copper substrates.

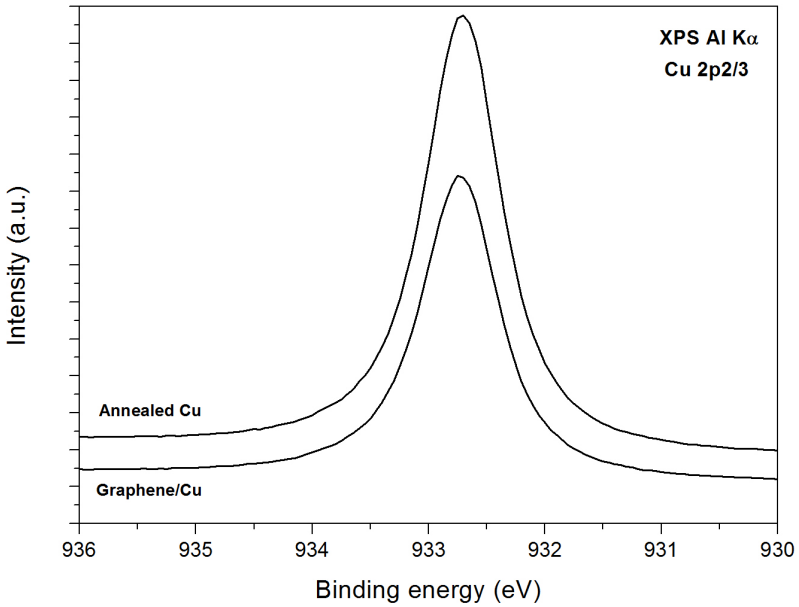

Sample	Height from base (counts)
Annealed Cu	228397
Graphene/Cu	159104
Difference	69293

Figure 30: High-resolution XPS spectra of the Cu $2p_{3/2}$ core level of a copper sample after the annealing step and after the growth step. The peak position is at 932.7 eV and the intensities are given in the table next to the spectra. The difference in intensity is due to the damping of the copper signal by means of the graphene overlayer. These spectra were recorded at a pass energy 3 eV.

3.3.6 XPS spectra of O 1s peak of Graphene sample after exposure and after treatment

The last XPS spectra displayed in Figure 31 shows the oxygen signal on the graphene/Cu sample after it has been exposed to air for two months and after the thermal treatment at 773 K. After air exposure there is a broad oxygen signal visible with two peaks.

These two peaks are assigned to oxygen in the carbonyl (C=O) group at 531.2 eV and in the hydroxyl (OH) group at 532.6 eV. The O 1s spectrum after the first thermal treatment exhibits one large peak at the hydroxyl component position and a small increase around the carbonyl group component. During this first treatment the graphene sample was heated to 773 K for 5 minutes in UHV. From this O 1s spectrum we can conclude that a heat treatment at 773 K was not sufficient to remove all the contaminations from the graphene surface. It is important to note that no significant oxygen signal was measured after the second treatment, were the temperature was increased to 973 K for five minutes.

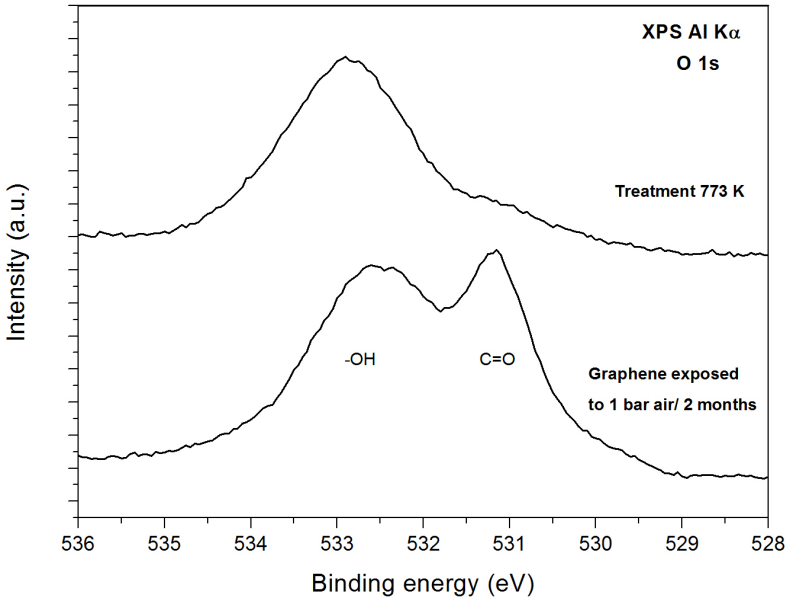

Element	Position
- OH	532.6 eV
C=O	531.2 eV

Figure 31: High-resolution XPS spectra of the O 1s core level region of a graphene sample after air exposure and after the first annealing to 773 K. Two main peaks are assigned to oxygen, the carbonyl (C=O) group at 531.2 eV and the hydroxyl (OH) group at 532.6 eV. These spectra were recorded at pass energy 6 eV.

From these measurements we can conclude that the first thermal treatment has only partly removed the oxygen contamination from the graphene surface. While the second treatment did succeed in the complete removal of oxygen species, it did however cause minor damage to the graphene sample, causing increase in the I_D/I_G ratio.

3.3.7 UPS and EELS measurements of annealed copper and graphene on Cu before/after air exposure and after thermal treatment

Besides in situ XPS measurements, UPS and EELS measurements were also performed during this thesis project, to detect changes of the electrical character, band bending and charge transfer of the valence band of our graphene samples. First, we are going to explain the obtained UPS spectra, afterwards we finish this chapter with analysing our EELS results.

Figure 32 compares the UPS valence band spectra of annealed Cu, graphene grown on Cu and graphene on copper after they have been exposed to an ambient environment. The UPS spectra were collected within 14 eV of the Fermi level located at the origin (0 eV). The UPS spectra of our annealed copper sample shows spectral features of the Cu-3d band for binding energies between 2-4 eV, with the Fermi edge at 0 eV and the 4s band visible in the range around 0-2 eV.

When we look at the graphene/copper spectrum we notice an overall decrease in the copper signal intensity. However the 3d band and the Fermi edge signal can still be distinguished. This decrease in intensity is due to the carbon deposition on top of the Cu substrate that damps the copper photoelectron intensity as described before. On the other hand, the main features of the Cu3d-band can clearly be recognized thus pointing to a rather weak interaction between the Cu support and the graphene layer on its top.

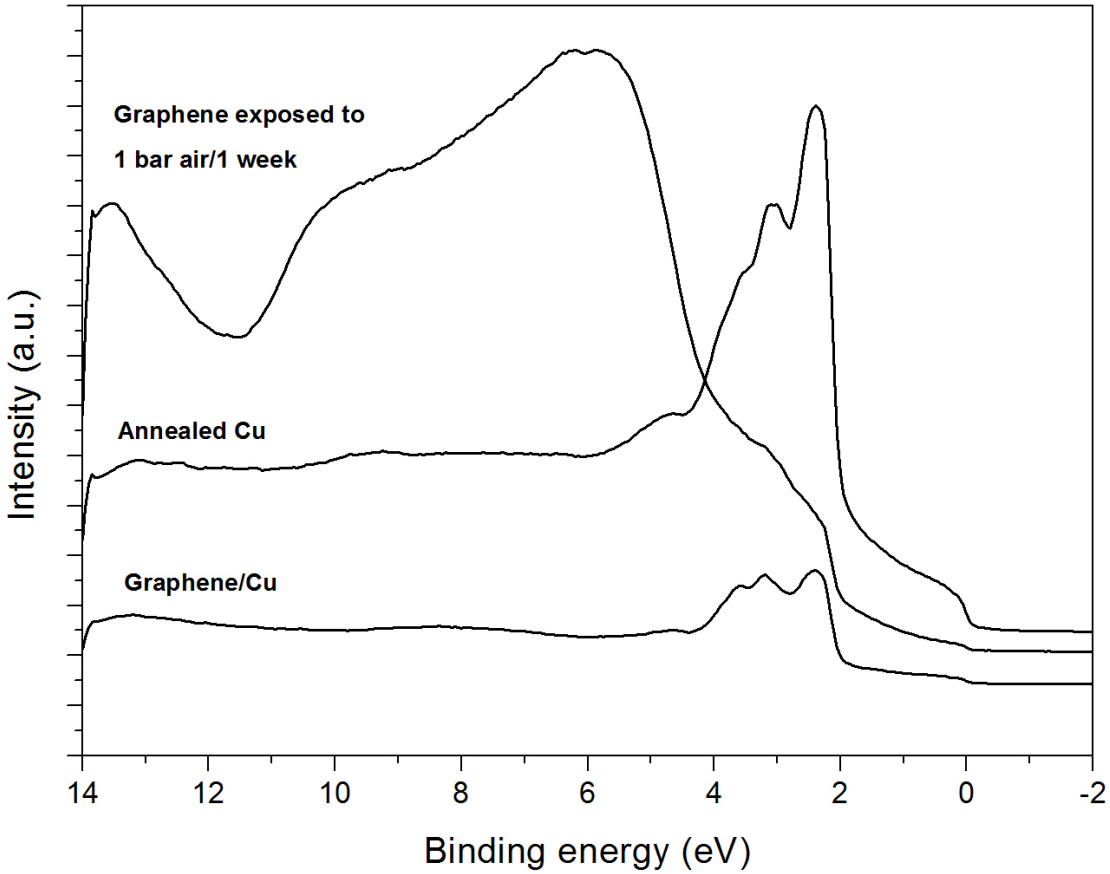

Figure 32: This figure shows UPS spectra of an annealed copper sample, graphene on copper sample and one graphene sample after it has been exposed to air for one week. In the annealed copper spectrum we can identify the 3d band at 2 eV, the Fermi edge at 0 eV and the plateau like 4s band between them. In the spectrum of one graphene sample we can see a small emission feature at 3 eV. This is caused by the π band state of graphene. These spectra were recorded at pass energy 3 eV.

In the UPS spectra of graphene, we also see a small emission feature at around 3 eV, which is not present in the spectrum acquired on the pure Cu substrate after annealing. Cho S.W. et al have shown that this increase is caused by the π band state of graphene. In other words this peak around 3 eV is characteristic for the carbon sp^2 hybridization in our graphene layer [38, 39].

After our graphene samples have been exposed to air for one week, the spectral features of Cu are no longer discernible thus pointing to a large amount of oxygen and carbon based adsorbates on top of the graphene. All the absorbed impurities affect the charge carriers, the electron mean free path and electron mobility within our graphene sample. Therefore, it is important to study the influence of an ambient environment on the graphene sample post growth. From these UPS data we can conclude that the valence band properties are probably very sensitive towards contaminations arising from exposure to air. **This means that graphene samples should be treated accordingly to removes such air-based contaminations before they graphene layers are studied or used in an application.**

As previously mentioned, EELS investigations also allow to deduce electronic structure information from the graphene sample. We measured different EELS spectra to evaluate the electronic properties of graphene/Cu samples under various conditions. Again the obtained EELS data were acquired from annealed copper samples, a HOPG sample, and graphene/copper samples before and after their air exposure to air as well as after the two thermal treatments.

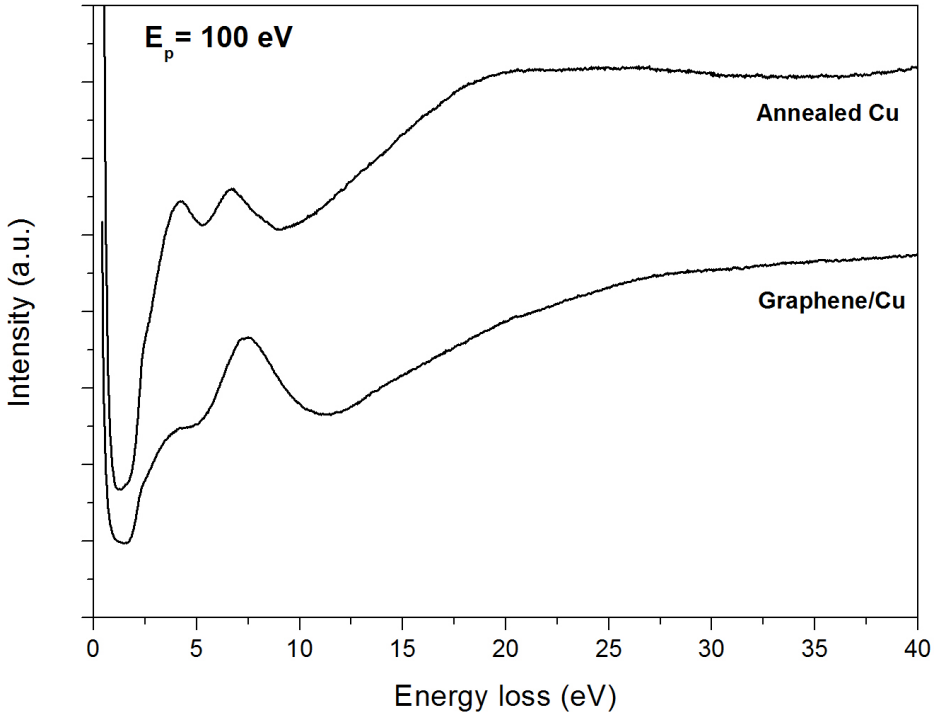

Figure 33: Low electron energy loss spectra of an annealed copper sample and graphene on copper sample. Both measurements were taken on the same spot on our graphene sample 5. A primary electron beam energy (Ep) of 100 eV and a constant pass energy (PE) of 3 eV were used to produce these spectra.

Figure 33 compares an EELS spectrum of clean copper after the annealing step to an EELS spectrum after the growth step of the CVD process. The low loss EELS spectrum of annealed copper shows two main components around 3 and 6 eV from the zero loss peak. Residues of these signals are still visible in the spectrum of our grown graphene sample but the largest peak position has shifted to the 7 eV. Raman measurements have shown that we made bilayer graphene on our samples. Therefore, we will associate this peak with plasmon excitation of the π valence band electrons, resulting from the sp^2 hexagonal crystal structure of graphene. Eberlein et al. have shown that the peak position of this plasmon can vary between 7 and 5 eV [40].

There are a major changes visible in the EELS spectra when our graphene samples were exposed to air for two months. Figure 34 shows the low loss EELS spectrum of graphene after air exposure. The main EELS feature of graphene at 7 eV is almost completely suppressed due to air contamination on the graphene surface. However, there are two slight increases in signal intensity around 5 and 8 eV. Langer et al. also observed these out of plane excitations and the damping of the signal in response to the absorbed contaminations [10, 41].

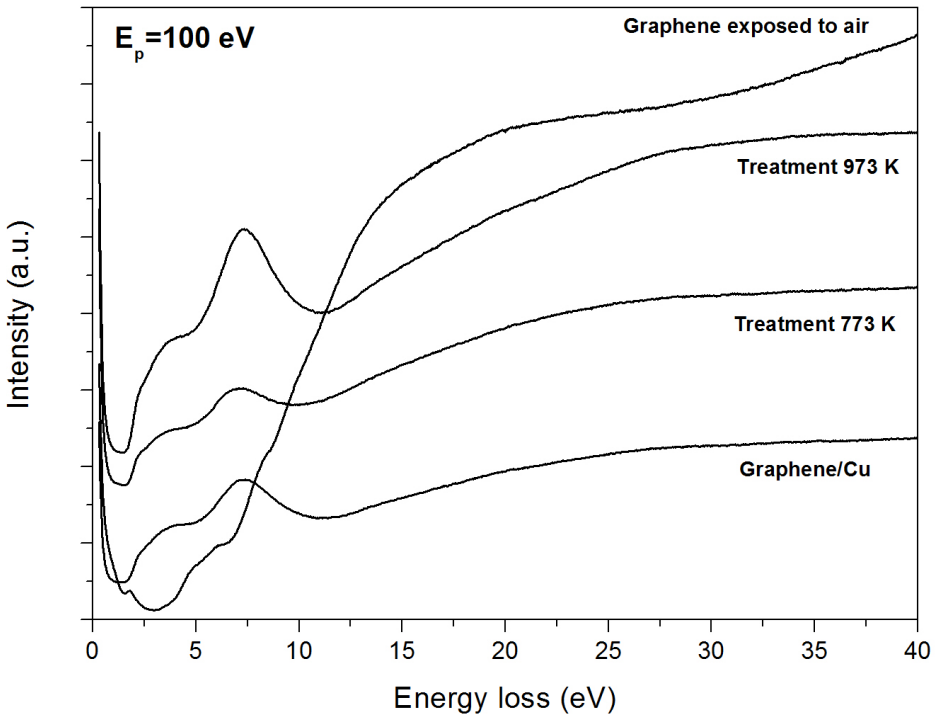

Figure 34: Low electron energy loss spectra of graphene on copper sample before and after air exposure as well as graphene samples after thermal treatments at 773 K and 973 K. Both measurements were taken on the same spot on our graphene sample 5. A primary electron beam energy (Ep) of 100 eV and a constant pass energy (PE) of 3 eV were used to produce these spectra.

Figure 34 also contain two EELS spectra obtained after the two thermal treatments. Our goal was to remove or largely decrease the amount of absorbed air contamination present on the sample surface. In the EELS spectrum of the first treatment, were the sample was heated to 773 K, the mean feature of the π- π* excitation reappears around 7 eV. When the temperature is further increased to 973 K during the second treatment the peak intensity increases further. However, we also notice that the intensity of the copper signal increases and we observe a small shift of the maximum position to the right. This small shift and an increase of copper signal indicate that small defects arise in the graphene layer at these high temperatures. Raman as well as XPS measurements have all shown the same result.

Chapter 4

Summary and outlook: There is more room in flatland

It has been ten years since graphene was first reported and in that time graphene has grown from an unexpected newcomer to a Nobel Prize winning star. During these ten years the research performed on graphene has risen exponentially, with newly produced articles and finding every day. This great interest proves that graphene has great potential for future applications and exciting new physics.

With this thesis project we wanted to take our first steps into graphene research. In the first part, we aimed on producing monolayer graphene on copper substrates using the CVD processes. The presented Raman measurements show that we succeeded in the production of high quality graphene using methane and hydrogen as precursors. The found CVD processes during this project produced single and bilayer graphene in samples 12 and 5. In these graphene films there was only a small percentage of defects present, indicated by an I_D/I_G ratio of 0.18 and 0.07. With this ratio and the Tuinstra Köning equation, we calculated that our graphene flakes in samples 12 and 5 had a diameter of more or less 75 and 197 nm. We obtained representative AFM images with interesting structures from our graphene samples. In these images the boundaries between the graphene flakes on Cu terraces were clearly visible. We also observed the presence of wrinkles or ripples on the copper terraces. These winkles and ripples caused by a difference in thermal expansion coefficient showed height differences between 0.5 and 0.8 nm in the line profiles. We concluded that our graphene flakes extended over different crystalline copper regions and that there were weak interactions present between this copper substrate and the graphene flakes.

In the second part of this project we wanted to investigate the original chemical character after growth as well as the shift in this chemical character after air exposure. First, we investigated wide scan XPS results to get an impression of the changes during the CVD process and after exposure to an ambient environment. In the survey scans we only saw minor changes. Afterwards we exanimated these effects in detail by measuring changes in the XPS core levels of C 1s, Cu $2p_{2/3}$ and O 1s elements. From the C 1s core level we learned that the main carbon of graphene on Cu is positioned at binding energy 284.7 eV (C_1 position), while that of HOPG is at 284.4 eV (C_2 position). We found that the C 1s peak shifts from the C_1 position towards C_2 position when the graphene samples are exposed to air. Kidambi P. et al. have reported that this shift can be caused by the interaction between the Cu substrate and graphene, due to charge transfer. Besides a shift in the C 1s peak, intercalation of oxygen also causes three additional signal increases in the C 1s spectrum. We assigned the first peak around 286.5 eV to alcohol (C-OH) groups, the second around 287.5 eV is caused by C=O groups and the third rises from the carbonyl (O-C=O) groups around 288.7 eV. From the measured damping effect of the Cu $2p_{2/3}$ spectra we could calculate that the thickness of our graphene layer was around 0.3 nm.

This agrees with the previous executed Raman measurements. Comparing in situ EELS and UPS measurements with ex situ ones, after air exposure, gave the same results. From all those spectroscopy studies we could conclude that the air exposure caused some major changes in graphene chemical character and consequently also in it extraordinary properties. The absorbed contaminations destroy the two-dimensional character of the graphene sheets.
As a final part in this project we tried to remove these surface contaminations. Therefore we tested two thermal treatments. During the first thermal treatment the samples were heated to 773 K and during the second one the temperature reached 973 K. After each thermal treatment, in situ XPS and EELS studies were performed. XPS spectra have shown that the first treatment already lowered the intensity of the O 1s but it did not remove all the contaminations from the graphene surface. After the second treatment, we could no longer detect an oxygen signal. Unfortunately, the higher temperature during second treatment also caused minor defects in the graphene sheets. This increase in defect density was measured by an increase in the D band on the Raman spectra and a shift of the C 1s peak in XPS results. EELS spectra showed that specific features of graphene reappeared after the treatments, but also in the EELS measurements we detected a small shift due to appeared defects in the graphene sheets. These defects are mainly caused by the previously mentioned difference in thermal expansion coefficient of copper and graphene. During the thermal treatment the rigid graphene cannot follow the expansion of the underlying copper substrate. This caused strain effect that lead to the detachment of the graphene, leaving spots of bare copper behind.

To summarize, we have proven that ambient air contaminations are found to introduce a major change in the chemical character of our produced graphene samples. Therefore, it is important to find a surface treatment that is easy to use and does not increase the prevalence of defects in the graphene crystal structure. The next step in the project would be to try a third treatment method. This treatment would use the temperature of the first treatment together with a hydrogen flow of 35 sccm. In this way we hope to remove all the oxygen from the surface, without causing an increase in defect density by operating at a lower temperature. Another opportunity appeared after we made sample 12 in the last week of this project. We expect that there will be differences in XPS, EELS and UPS measurements between bilayer and monolayer graphene. It would be interesting to investigate these differences. These results could prove what has already been discovered, that in the Angstrom range very small changes, can eventually lead to major difference in fundamental properties.

Appendix

This Appendix contains all the used CVD processes with their parameters and the corresponding Raman measurements.

4.1 CVD process different samples

Table 5 summarizes all the tested CVD processes with the used parameters for each sample. Afterwards we measure Raman spectra of all these samples, those results are given in the next part.
During this thesis project we had some problems with estimating the temperature inside the CVD reactor. We could not measure the absolute temperature with the use of a pyrometer. We did however notice that the samples melted when the applied power passed 410 Watt. Therefore we mentioned the applied power for each CVD process instead of the temperature.

Table 5: overview table of all the used CVD processes with different heating times and gas flows.

Sample Nr.	Power (Watt)	Heating (min)	Annealing (min)	Annealing (sccm)	Growing (min)	Growing (sccm)	Cooling (min)	Cooling (sccm)
1	391	10	20	/	4	35 CH_4	10	/
2	393	10	30	/	10	100 CH_4	10	/
3								
4	401	12	15	35 H_2	25	50 H_2 20 CH_4	6	/
5	394	10	20	35 H_2	30	50 H_2 20 CH_4	4	35 H_2
6 Annealed copper	392	10	40	35 H_2	/	/	4	35 H_2
7	380	10	20	35 H_2	30	50 H_2 10 CH_4	4	50 H_2
8	388	10	20	35 H_2	30	50 H_2 10 CH_4	4	50 H_2 10 CH_4
9	256	10	20	35 H_2	35	50 H_2 20 CH_4	4	35 H_2
12	309	10	25	35 H_2	40	50 H_2 20 CH_4	4	35 H_2

After we formed sample 8 we made some adjustments to the set-up lowering the resistivity. These adaptions lowered the needed power to reach the Cu melting point. Consequently the needed power to produce sample 9 was much lower than with all the other CVD processes.

4.2 Raman measurements different samples

Graphene sample 1 on Cu and on Si

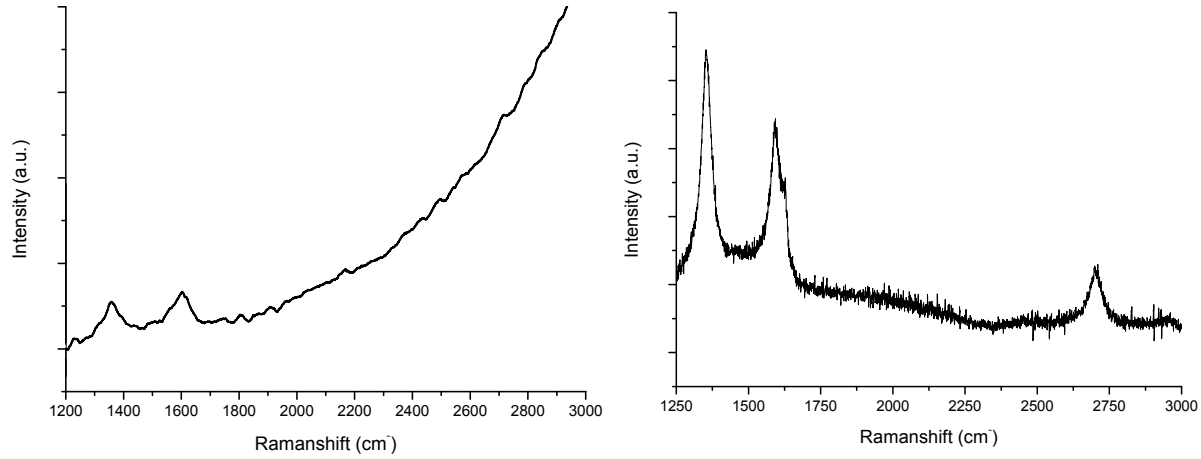

Figure 35: Two Raman spectra obtained from our graphene sample 1 (λ = 488nm) on copper (upper graph) and after transfer to SiO_2 (lower graph). On copper only the D band and G band are visible. After the transfer three peaks can be distinguished. The D peak and G peak have a higher intensity and the 2D peak has appeared. The measurements are performed with the following parameters: objective magnification: x50, 2x20 s (left graph) measuring time and objective magnification: x100, 2x120 s (right graph) measuring time.

Graphene sample 2 (only CH_4)

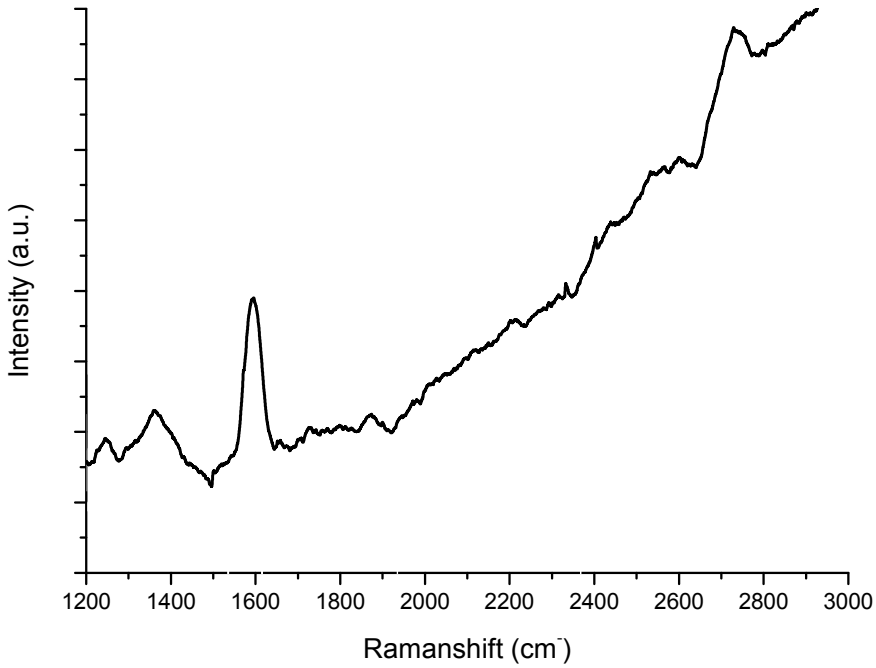

Figure 36: A Raman spectrum obtained from graphene sample 2 (λ = 488nm) on copper. The D band (1364 cm^-) and G band (1597 cm^-) are clearly visible, while the 2D band is less pronounced. The Raman measurements are performed with the following parameters: objective magnification: x50; 2x20 s measuring time.

Graphene sample 3 on SiO_2 substrate

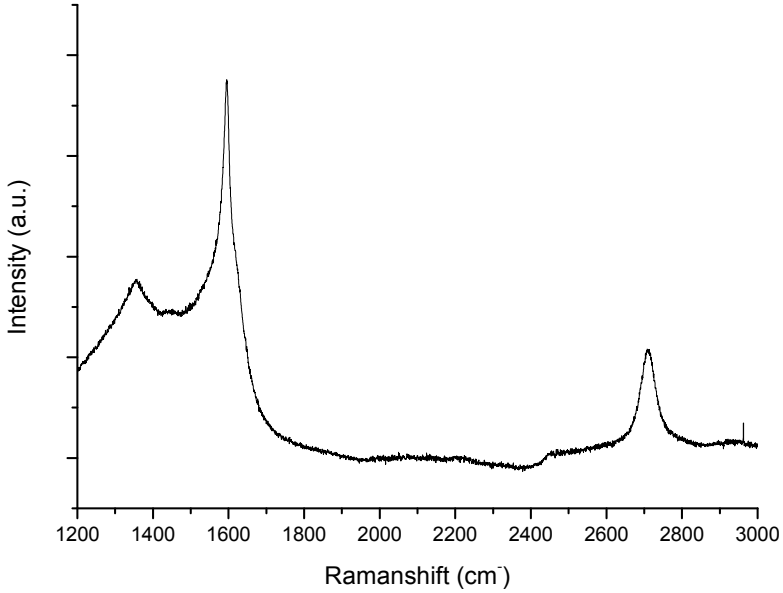

Figure 37: A Raman spectrum obtained from graphene sample 3 (λ = 488nm) on a SiO_2 substrate. The D band (13543 cm^-), the G band (1595 cm^-) and the 2D band (2708 cm^-) are all visible. The Raman measurements are performed with the following parameters: objective magnification: x100; 5x60 s measuring time.

Graphene sample 4 on Cu

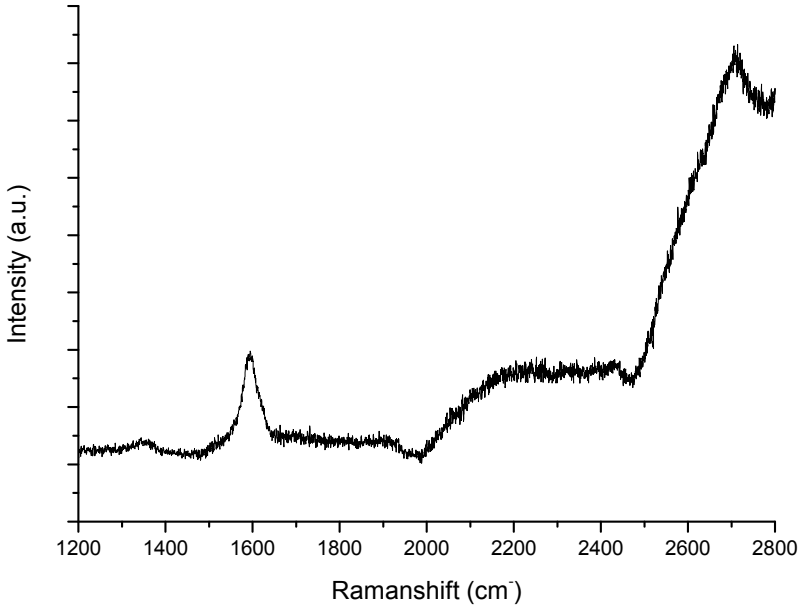

Figure 38: A Raman spectrum obtained from graphene sample 2 (λ = 488nm) on copper. The D band (1355 cm^-) is small and G band as well as the 2D are visible at 1580 cm^- and 2711 1580 cm^-. The Raman measurements are performed with the following parameters: objective magnification: x50; 5x60 s measuring time.

Graphene sample 5 before treatment

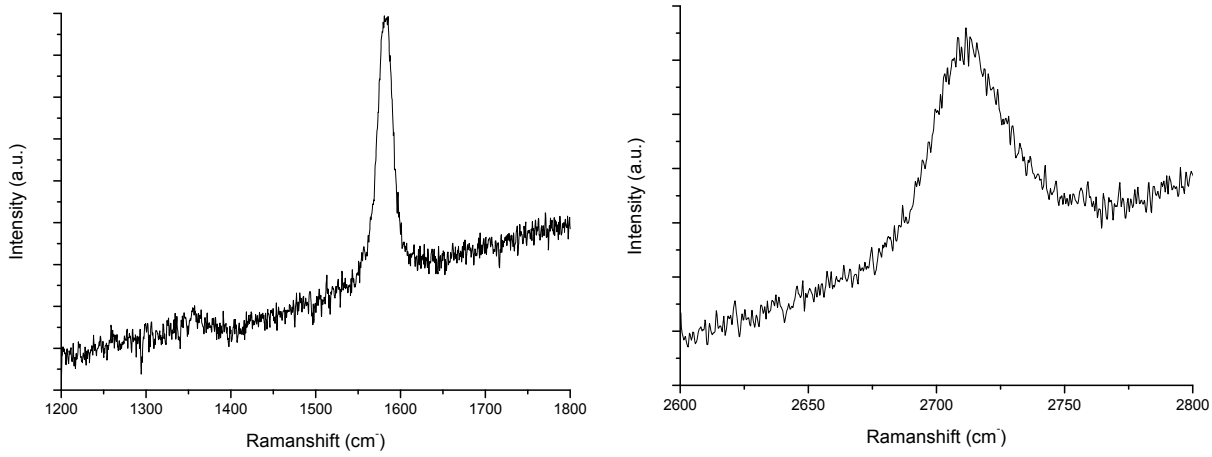

Figure 39: A typical Raman spectrum obtained from a graphene on Cu sample (λ = 488nm). Small D (1357 cm^{-}) band contribution points towards a very low amount of defects. The high G peak (1580.9 cm^{-}) and 2D peak (2711 cm^{-}) indicate the formation of 1 to 2 layered graphene samples. The Raman measurements are performed with the following parameters: objective magnification: x100; 3x120 s measuring time.

Graphene sample 5 after treatment

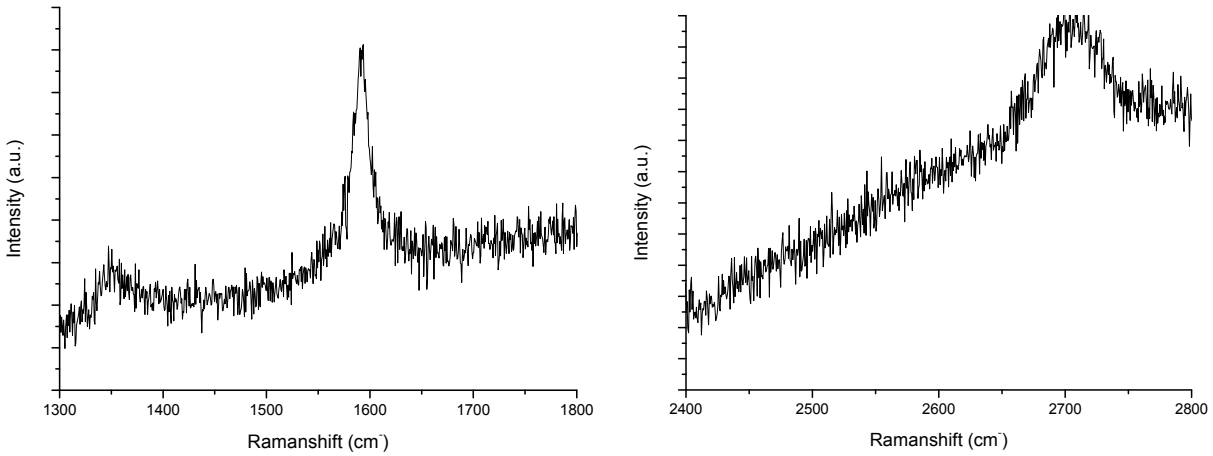

Figure 40: A Raman spectrum obtained from a graphene on Cu sample after thermal treartment of 773 K and 973 K (λ = 488nm). The increased D (1347 cm^{-}) band points towards a small increase in the amount of defects. The high G peak (1593.6 cm^{-}) and 2D peak (2694.3 cm^{-}) indicate the formation of 1 to 2 layered graphene samples. The Raman measurements are performed with the following parameters: objective magnification: x50; 3x120 s measuring time.

Sample 6 annealed Cu

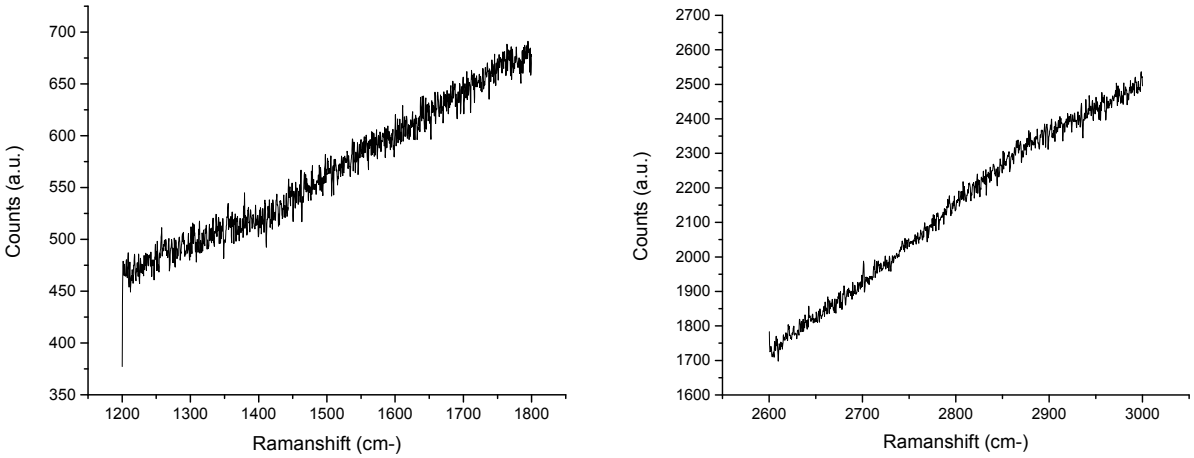

Figure 41: A typical Raman spectrum obtained from an annealed Cu foil (λ = 488 nm). There are no visible D, G or 2D bands present. Only the high background signal is visible in these spectra. The Raman measurements are performed with the following parameters: objective magnification: x100; 3x120 s measuring time.

Graphene sample 7 on Cu

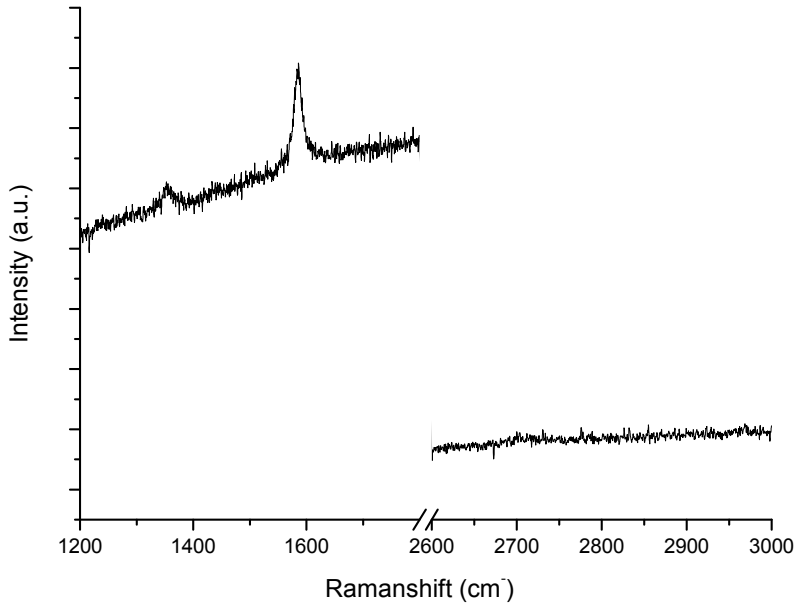

Figure 42: A Raman spectrum obtained from graphene sample 7 (λ = 488nm) on copper. The D band (1353.4 cm^{-}) and G band (1586.2 cm^{-}) are clearly visible, while the 2D band not visible. The Raman measurements are performed with the following parameters: objective magnification: x100; 3x120 s measuring time.

Graphene sample 8 on Cu

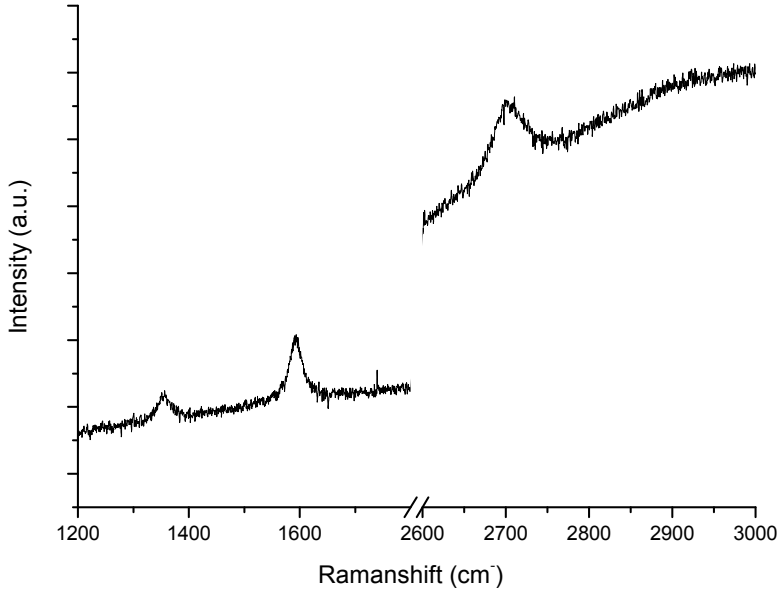

Figure 43: A Raman spectrum obtained from graphene sample 8 (λ = 488nm) on copper. The D band (1356.5 cm^{-}) and G band (1593 cm^{-}) are clearly visible, while the 2D band (2698 cm^{-}) is less pronounced. The Raman measurements are performed with the following parameters: objective magnification: x100; 3x120 s measuring time.

Graphene sample 9 on Cu

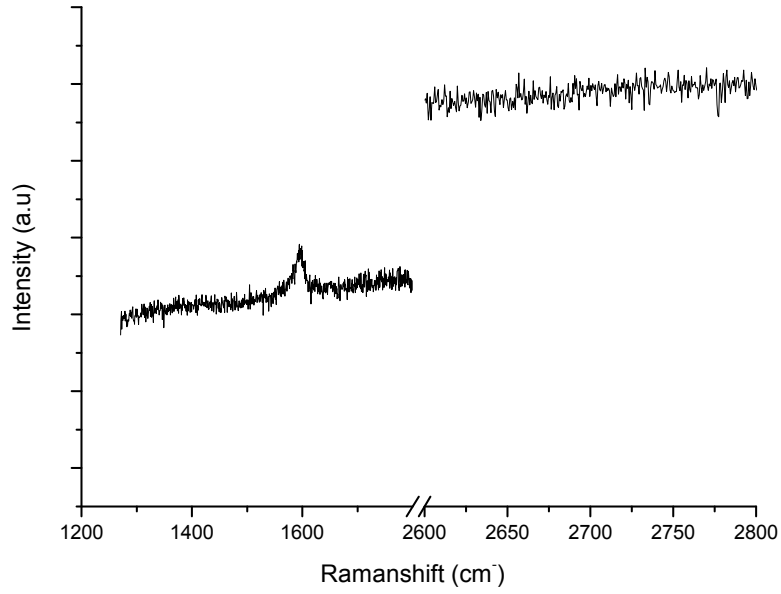

Figure 44: A Raman spectrum obtained from graphene sample 9 (λ = 488nm) on copper. Only the G band at 1592 cm^{-} is clearly visible, while the D and 2D band are not detected. The Raman measurements are performed with the following parameters: objective magnification: x100; 3x120 s measuring time.

HOPG sample

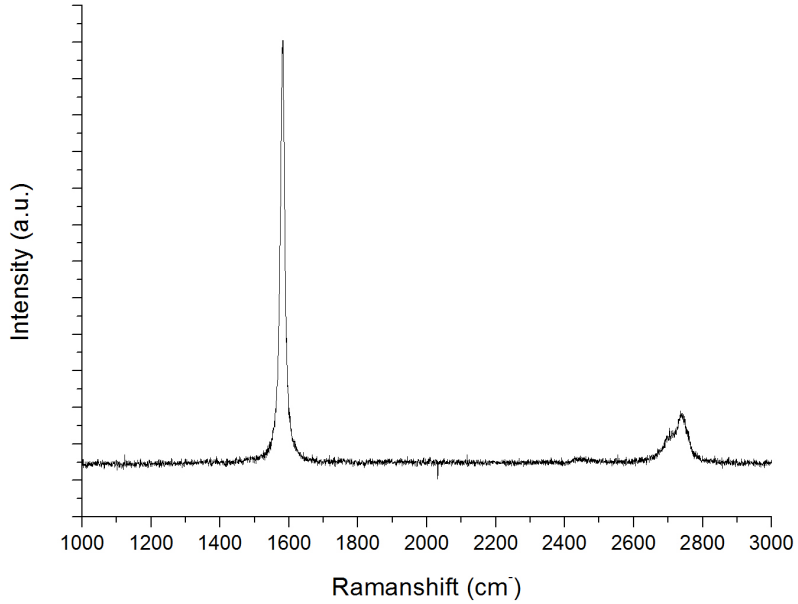

Figure 45: A typical Raman spectrum obtained from a HOPG sample (λ = 488 nm). These spectra show a strong G band at 1580 cm- and a wide 2D band around 2700 cm-. The Raman measurements are performed with the following parameters: objective magnification: x100; 3x120 s measuring time.

Graphene sample 12 on Cu

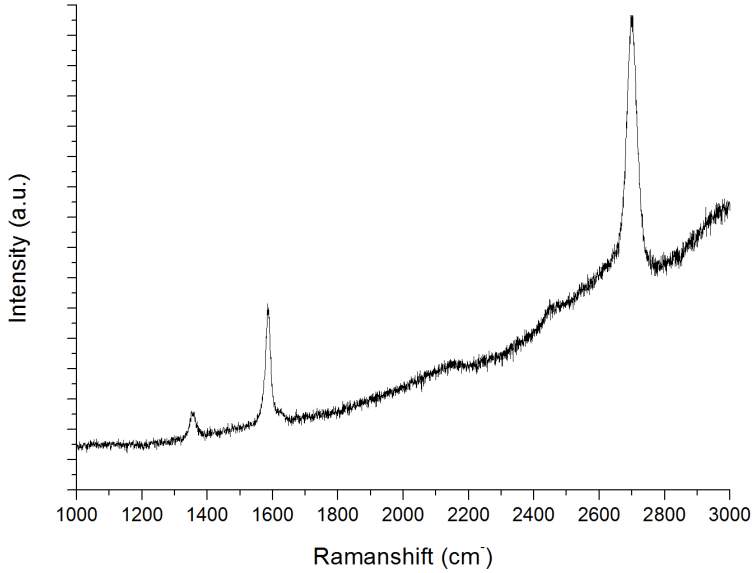

Figure 46: A Raman spectra of the produced single layer graphene in sample 12 (λ = 488nm) on copper. The D band at 1351.4 cm- is rather small. While G band as well as a large 2D are located at 1584.7 cm- and 2696.6 cm-. The Raman measurements are performed with the following parameters: objective magnification: x100; 3x120 s measuring time.

References

1. The rise and rise of graphene. Nature Nanotechnology. 2010;5(11):755-.
2. Geim AK, Novoselov KS. The rise of graphene. Nature Materials. 2007;6(3):183-91.
3. Geim AK. Graphene: Status and Prospects. Science. 2009;324(5934):1530-4.
4. Katsnelson MI. Graphene: carbon in two dimensions. Materials Today. 2007;10(1-2):20-7.
5. Avouris P, Dimitrakopoulos C. Graphene: synthesis and applications. Materials Today. 2012;15(3):86-97.
6. Rao CNR, Sood AK, Subrahmanyam KS, Govindaraj A. Graphene: The New Two-Dimensional Nanomaterial. Angewandte Chemie-International Edition. 2009;48(42):7752-77.
7. Tian J, Hu B, Wei Z, Jin Y, Luo Z, Xia M, et al. Surface structure deduced differences of copper foil and film for graphene CVD growth. Applied Surface Science. 2014;300:73-9.
8. Ge W, Lu B, Li WJ, Lu JG, Ye ZZ. Synthesis of graphene together with undesired CuxO nanodots on copper foils by low-pressure chemical vapor deposition. Vacuum. 2013;97:9-14.
9. Kidambi PR, Bayer BC, Blume R, Wang Z-J, Baehtz C, Weatherup RS, et al. Observing Graphene Grow: Catalyst-Graphene Interactions during Scalable Graphene Growth on Polycrystalline Copper. Nano Letters. 2013;13(10):4769-78.
10. Siokou A, Ravani F, Karakalos S, Frank O, Kalbac M, Galiotis C. Surface refinement and electronic properties of graphene layers grown on copper substrate: An XPS, UPS and EELS study. Applied Surface Science. 2011;257(23):9785-90.
11. Allen MJ, Tung VC, Kaner RB. Honeycomb Carbon: A Review of Graphene. Chemical Reviews. 2010;110(1):132-45.
12. Geim A. http://www.graphene.manchester.ac.uk/story/properties/.
13. Novoselov KS, Geim AK, Morozov SV, Jiang D, Zhang Y, Dubonos SV, et al. Electric field effect in atomically thin carbon films. Science. 2004;306(5696):666-9.
14. Zhong H, Xu K, Liu Z, Xu G, Shi L, Fan Y, et al. Charge transport mechanisms of graphene/semiconductor Schottky barriers: A theoretical and experimental study. Journal of Applied Physics. 2014;115(1).
15. Li XS, Cai WW, An JH, Kim S, Nah J, Yang DX, et al. Large-Area Synthesis of High-Quality and Uniform Graphene Films on Copper Foils. Science. 2009;324(5932):1312-4.
16. Mattevi C, Kim H, Chhowalla M. A review of chemical vapour deposition of graphene on copper. Journal of Materials Chemistry. 2011;21(10):3324-34.
17. Munoz R, Gomez-Aleixandre C. Review of CVD Synthesis of Graphene. Chemical Vapor Deposition. 2013;19(10-12):297-322.
18. Bae S, Kim H, Lee Y, Xu X, Park J-S, Zheng Y, et al. Roll-to-roll production of 30-inch graphene films for transparent electrodes. Nature Nanotechnology. 2010;5(8):574-8.
19. Congqin M, Churan Z, Owen L, Ya-Hong X. Chemical vapor deposition of graphene. In: Mikhailov DS, editor. Physics and Applications of graphene - Experiments: InTech; 2011. p. 540.
20. Ma L, Ren W, Dong Z, Liu L, Cheng H. Progress of graphene growth on copper by chemical vapor deposition: Growth behavior and controlled synthesis. Chinese Science Bulletin. 2012;57(23):2995-9.
21. Bhaviripudi S, Jia X, Dresselhaus MS, Kong J. Role of Kinetic Factors in Chemical Vapor Deposition Synthesis of Uniform Large Area Graphene Using Copper Catalyst. Nano Letters. 2010;10(10):4128-33.
22. Moulder JF, Stickle WF, Sobol PE, Bomben KD. Handbook of X-ray Photoelectron Spectroscopy. Minnesota, United States of America: ULVAC-PHI, Inc.; 1996.
23. Seah MP, Briggs D, Rivière JC, Hofmann S, Sherwood PMA, Waddington SD. Practical surface analysis - Auger and X-ray photoelectron spectroscopy. Briggs D, Seah MP, editors. England: WILEY; 1996.
24. Egerton RF. Electron Energy-Loss Spectroscopy in the Electron Microscope. Third ed. Egerton RF, editor. Londen: Springer; 2011. 431 p.
25. Suenaga K, Sandre E, Colliex C, Pickard CJ, Kataura H, Iijima S. Electron energy-loss spectroscopy of electron states in isolated carbon nanostructures. Physical Review B. 2001;63(16).
26. Dufrêne Y. Life at the nanoscale atomic force microscopy of live cells: Singapore Pan Stanford Publishing; 2011.
27. Meyer E, Wiesendanger R, Morita S. Noncontact atomic force microscopy: Berlin Springer; 2002.

28. Schrader B. Infrared and raman spectroscopy methods and applications: Weinheim VCH; 1995.
29. Colthup NB, Wiberley SE, Daly LH. Introduction to infrared and Raman spectroscopy: Boston Academic Press 3; 1990.
30. Kidambi PR, Ducati C, Dlubak B, Gardiner D, Weatherup RS, Martin M-B, et al. The Parameter Space of Graphene Chemical Vapor Deposition on Polycrystalline Cu. Journal of Physical Chemistry C. 2012;116(42):22492-501.
31. Malard LM, Pimenta MA, Dresselhaus G, Dresselhaus MS. Raman spectroscopy in graphene. Physics Reports-Review Section of Physics Letters. 2009;473(5-6):51-87.
32. Ferrari AC. Raman spectroscopy of graphene and graphite: Disorder, electron-phonon coupling, doping and nonadiabatic effects. Solid State Communications. 2007;143(1-2):47-57.
33. Costa SD, Righi A, Fantini C, Hao Y, Magnuson C, Colombo L, et al. Resonant Raman spectroscopy of graphene grown on copper substrates. Solid State Communications. 2012;152(15):1317-20.
34. Ferrari AC, Meyer JC, Scardaci V, Casiraghi C, Lazzeri M, Mauri F, et al. Raman spectrum of graphene and graphene layers. Physical Review Letters. 2006;97(18).
35. Zhao L, Rim KT, Zhou H, He R, Heinz TF, Pinczuk A, et al. Influence of copper crystal surface on the CVD growth of large area monolayer graphene. Solid State Communications. 2011;151(7):509-13.
36. Zhang Y, Gao T, Gao Y, Xie S, Ji Q, Yan K, et al. Defect-like Structures of Graphene on Copper Foils for Strain Relief Investigated by High-Resolution Scanning Tunneling Microscopy. Acs Nano. 2011;5(5):4014-22.
37. Streubel P, Hesse R, Makhova L, Schindelka J, Denecke R. a practicable method for thickness estimation of ultra thin layers from XPS date with UNIFET 20112011; 15 p.:[1-5 pp.].
38. Cho SW, Choi WM, Yi Y, Kang SJ. Interfacial electronic structure at metal/graphene contact. Current Applied Physics. 2011;11(4):S78-S80.
39. Cho SW, Yi Y, Kang SJ. The interfacial electronic structure between pentacene and multilayer graphene. Synthetic Metals. 2011;161(21-22):2488-91.
40. Bangert U, Eberlein T, Nair RR, Jones R, Gass M, Bleloch AL, et al. STEM plasmon spectroscopy of free standing graphene. Physica Status Solidi a-Applications and Materials Science. 2008;205(9):2265-9.
41. Langer T, Pfnuer H, Schumacher HW, Tegenkamp C. Graphitization process of SiC(0001) studied by electron energy loss spectroscopy. Applied Physics Letters. 2009;94(11).

Auteursrechtelijke overeenkomst

Ik/wij verlenen het wereldwijde auteursrecht voor de ingediende eindverhandeling:
Synthesis and in situ characterization of graphene on copper substrates

Richting: **master in de biomedische wetenschappen-bio-elektronica en nanotechnologie**
Jaar: **2014**

in alle mogelijke mediaformaten, - bestaande en in de toekomst te ontwikkelen - , aan de Universiteit Hasselt.

Niet tegenstaand deze toekenning van het auteursrecht aan de Universiteit Hasselt behoud ik als auteur het recht om de eindverhandeling, - in zijn geheel of gedeeltelijk -, vrij te reproduceren, (her)publiceren of distribueren zonder de toelating te moeten verkrijgen van de Universiteit Hasselt.

Ik bevestig dat de eindverhandeling mijn origineel werk is, en dat ik het recht heb om de rechten te verlenen die in deze overeenkomst worden beschreven. Ik verklaar tevens dat de eindverhandeling, naar mijn weten, het auteursrecht van anderen niet overtreedt.

Ik verklaar tevens dat ik voor het materiaal in de eindverhandeling dat beschermd wordt door het auteursrecht, de nodige toelatingen heb verkregen zodat ik deze ook aan de Universiteit Hasselt kan overdragen en dat dit duidelijk in de tekst en inhoud van de eindverhandeling werd genotificeerd.

Universiteit Hasselt zal mij als auteur(s) van de eindverhandeling identificeren en zal geen wijzigingen aanbrengen aan de eindverhandeling, uitgezonderd deze toegelaten door deze overeenkomst.

Voor akkoord,

Callens, Lien

Datum: **11/06/2014**